Chapter 8
Nanomechanical Characterization of Metallic Materials

Takahito Ohmura

8.1 Nanomechanical Characterization as an Advanced Technique

Macroscopic mechanical testing provides information on the mechanical response of materials to applied stress under various conditions. These mechanical properties are necessary for material design in engineering applications, and they are required on the scale between millimeters and meters. However, the origins in microstructures are controlled on a scale of micrometers, with the resolution in nanometers. The gap between these scales is remarkable 10^6 orders, and the gap is an extremely big hurdle in aiming at understanding the strengthening mechanism and improving the performance of structural materials.

Another big hurdle is the relation between microstructures and their mechanical properties. The macroscopic properties include the overall behavior of the material as an average quantity, but the deformation volume comprises distribution of stress and strain induced by geometrical inhomogeneity, including microstructure of materials. Although yield stress is extremely important for engineering purposes, the yielding phenomenon on a small scale, the so-called "micro-yielding," as an elemental step of macroscopic yielding, is still unrevealed. Physical models of mechanical behavior on small scales have been utilized to understand and/or predict the mechanical properties of metallic materials. The microstructures on nanometer to micrometer scale can be observed in detail with the most advanced observation apparatus, but it is still challenging to measure the mechanical behavior on the scale same as that used in the observation. As a method for describing plastic deformation quantitatively, we often

T. Ohmura (✉)

Research Center for Structural Materials, National Institute for Materials Science, Tsukuba, Japan
e-mail: ohmura.takahito@nims.go.jp

Center for Elements Strategy Initiative for Structural Materials (ESISM), Kyoto University, Sakyo-ku, Kyoto 606-8501, Japan

use the dislocation theory; however, it is extremely difficult to measure the stress–strain relations directly associated with dislocation dynamics and evolution even if we can observe the behavior of individual dislocations with electron microscopes experimentally. Thus, the elucidation of the dynamic behavior of the relations, as well as removing the 10^6 order gap, is important.

Nanoindentation and micropillar testing are techniques that can be used to measure the dynamic behavior on the nanometer scale.

The nanoindentation method penetrates an indenter into a sample surface under a load of μN resolution and measures the penetration depth in nm unit, to evaluate the elastoplastic deformation of materials. The depth of the indent marks is typically below 100 nm and less than a micron horizontally. The depth is measured using a displacement gage, and then converted into the contact area by using the indenter's geometry. It can be called, in particular, depth-sensing indentation, based on the measurement principle. The details of this technique are available in the literature (Nishibori and Kinoshita 1997, 1978; Newey et al. 1982; Loubet et al. 1984; Doerner and Nix 1986; Oliver and Pharr 1992; Tsui et al. 1996; Bolshakov and Pharr 1998; Lim and Chaudhri 1999; Nix and Gao 1998; McElhaney et al. 1998; Ohmura and Tsuzaki 2007a).

Micropillar testing is a technique of uniaxial loading in compression of a columnar-shaped specimen of 100 nm–μm in diameter, typically inside the chamber of a scanning electron microscope (SEM) or a transmission electron microscope (TEM), for its in situ straining. The advanced technique is to measure the load–displacement data during staining, which provides a direct relation between microstructural evolution and mechanical behavior. In the conventional TEM in situ testing, an important point lies in observing the motion of the dislocation and microstructure evolution; however, the advanced technique is developed to measure the dynamic mechanical behavior at the same time.

In this chapter, applications of the nanomechanical characterization are described, and an elemental step and strengthening factors for the macroscopic properties are discussed.

8.2 Plasticity Initiation Analysis Through Nanoindentation Technique

A major merit of the nanoindentation technique is that it can measure less than micrometer sizes, as described above; another advantage is the fact that the underlying and fundamental behavior can be analyzed in the process of loading and unloading through consecutive measurement during the deformation. A representative example is the displacement burst phenomenon, the so-called "pop-in" event, which mostly appears in the loading process (Ohmura et al. 2001, 2002; Gerberich et al. 1996; Zbib and Bahr 2007; Ohmura and Tsuzaki 2007b, 2008; Masuda et al. 2020). Figure 8.1 shows a typical load–displacement curve for the Fe alloy, where

Fig. 8.1 Typical load–displacement curve for Fe alloy showing pop-in phenomenon on the loading curve, indicated by the dashed-line arrow
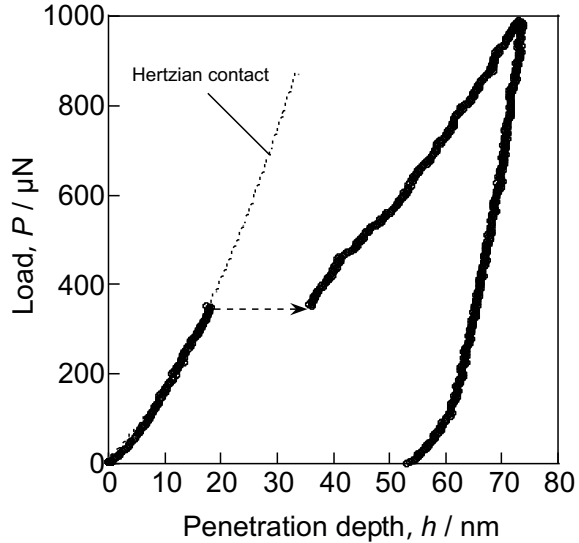
the pop-in phenomenon is indicated on the loading curve through the dashed-line arrow. The curve is obtained in the load-controlled mode, and the displacement burst is understood as a sudden drop in resistance to plastic deformation. When the same phenomenon is measured in the displacement-controlled mode, it appears as a sudden drop in the load (Ohmura et al. 2001). It is a drastic phenomenon to occur in a time shorter than 0.005 s, as the load–displacement data are captured 200 times per second and no point is recorded during the pop-in event.

At the beginning of the discovery of this phenomenon, it was noted that breaking a native oxide film on a sample surface might be a major reason for the event (Gerberich et al. 1996), but subsequently, it was found that the same phenomenon occurred in even noble metals such as gold, with much higher resistance to be oxidized (Ohmura et al. 2001). Additionally, the frequency of the event was higher in a sample with lower initial dislocation density, even in the same material (Ohmura et al. 2002; Zbib and Bahr 2007). Therefore, this phenomenon is considered an essential and elemental behavior of plastic deformation in materials.

Note that the pop-in phenomenon corresponds to transition from elastic to elasto-plastic deformation, and the shear stress underneath the indenter that is calculated from the applied load is close to the value of the order of the ideal strength (Gould-stone et al. 2000). This is described quantitatively, as follows, with Fig. 8.1 as an example. When we define P_c as a critical load for a pop-in event, the load–displacement curve that is lower than P_c fits very well with the dashed line of the Hertz contact model (Johnson 1985), given as

$$P = \frac{4}{3} E^* R^{\frac{1}{2}} h^{\frac{3}{2}}, \tag{8.1}$$

where R is the curvature of the indenter tip and E^* is the reduced modulus, given as

$$\frac{1}{E*} = \frac{1 - v_i^2}{E_i} + \frac{1 - v_s^2}{E_s}, \tag{8.2}$$

where E and v are Young's modulus and Poisson's ratio, respectively, and the subscripts i and s refer to the indenter and sample, respectively. This result clearly indicates that the deformation before the pop-in event is dominated by purely elastic deformation. In addition, the maximum shear stress underneath the indenter, τ_{max}, is given as follows:

$$\tau_{max} = 0.18 \left(\frac{E^*}{R} \right)^{\frac{2}{3}} P^{\frac{1}{3}}. \tag{8.3}$$

When $P_c = 350$ μN, from Fig. 8.1, as P is substituted into Eq. (8.3), τ_{max} is calculated as 11.3 GPa, which is approximately 1/7th the shear modulus of 83 GPa on the order of the ideal strength. This result indicates that the pop-in phenomenon corresponds to the plasticity initiation by dislocation nucleation from a region with no pre-existing lattice defect. On the other hand, a previous study conducted using the TEM in situ straining technique revealed that, in pure Al, dislocations are nucleated prior to the pop-in event (Minor et al. 2006). This indicates that some other processes, such as dislocation multiplication, occur subsequent to the dislocation nucleation to occur a pop-in event.

As an example of how the multiplication process of dislocations is related to the mechanical behavior, the results of TEM in situ compression deformation are shown. The specimen is pillar shaped for the compression test of Fe -3 wt% Si single crystal, with the compression axis being parallel to the <110> axis. By measuring the load–displacement relation during compression deformation simultaneously, the mechanical response and dislocation structure change can be synchronized. Figure 8.2 is a snapshot extracted from the recorded movie and shows the change in the dislocation structure during deformation (Ohmura et al. 2012). Figure 8.2a shows the snapshot right before the pop-in event, and (b) corresponds to that immediately after the pop-in event. In (b), an increase in the dislocation density is clearly observed, indicating that a multiplication of dislocations occurs during the pop-in event. The time difference between (a) and (b) is 1/30 s, indicating that the dislocation multiplication and propagation occur within a very short period. Figure 8.2c shows the load–displacement curve measured during TEM in situ straining, where the dashed arrow indicates a sudden drop in the load at the moment of pop-in. As this experiment was conducted in the displacement-controlled mode, the behavior is different from that of the displacement burst, which appears in the load-controlled mode; however, both of them show a drastic decrease in the deformation resistance, and thus can be regarded as essentially the same phenomena. This result indicates that dislocation multiplication is an important elementary process in deformation behavior, where

(a)

(b)

(c)
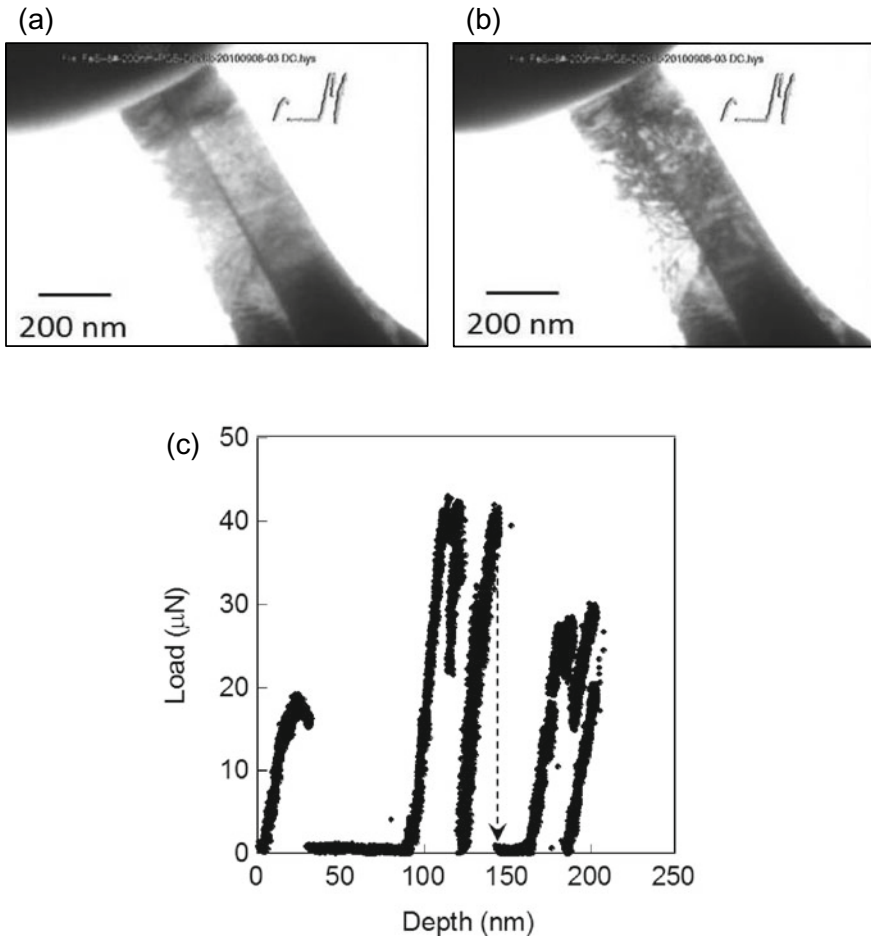
Fig. 8.2 Snapshot extracted from the recorded movie, showing changes in the dislocation structure during deformation. **a** Shows the snapshot right before the pop-in and **b** corresponds to the snapshot immediately after the pop-in. **c** Load–displacement curve measured during TEM in situ straining (Ohmura et al. 2012). Reprinted with permission from [T. Ohmura, L. Zhang, K. Sekido and K. Tsuzaki: J. Mater. Res., 27 (2012), 1742–1749.] Copyright (2012) by Cambridge University Press

the plastic strain increases rapidly. The relation between the evolution of dislocation structure and plastic strain is discussed further in Sect. 8.4.

To further understand the factors governing the initiation behavior of local plastic deformation, a systematic analysis was performed using various single crystals with a variety of materials with different crystal structures. All vertical directions of the sample surface were oriented to <001> . Figure 8.3 shows the relation between the maximum shear stress τ_{max}, calculated from the pop-in load P_c using Eq. (8.3), and the stiffness modulus G, converted from Young's modulus calculated from the

Fig. 8.3 Relationship between the maximum shear stress τ_{max} calculated from the pop-in load P_c using Eq. (8.3) and the stiffness modulus G converted from the Young's modulus calculated from the unloading curve (Ohmura et al. 2012). Reprinted with permission from [T. Ohmura, L. Zhang, K. Sekido and K. Tsuzaki: J. Mater. Res., 27 (2012), 1742–1749.] Copyright (2012) by Cambridge University Press
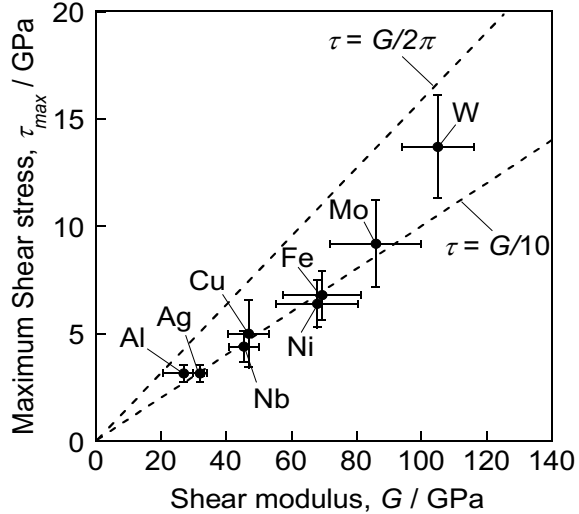
unloading curve (Ohmura et al. 2012). This relation was linear for all measured materials, and the coefficient was found to be close to $1/2\pi$.

On the other hand, one of the models in which the frictional stress of the perfect crystal on the slip plane was formulated is given as

$$\tau = \frac{b}{h}\frac{G}{2\pi}\sin\left(\frac{2\pi x}{b}\right), \tag{8.4}$$

where b is the magnitude of the Burgers vector, h is the distance between the slip planes, and x is the relative displacement in the slip direction. The maximum stress obtained by approximating b to h is $G/2\pi$ when $x = b/4$. This value is very close to that obtained experimentally in Fig. 8.3. This result strongly evidences that the stress level at which the pop-in behavior appears is close to the ideal strength regardless of the crystal structure, indicating that the critical stress strongly depends on the local shear modulus.

8.3 Effect of Lattice Defects Including Grain Boundaries, Solid-Solution Elements, and Initial Dislocation Density on the Plasticity Initiation Behavior

8.3.1 Grain Boundary

The model of grain refinement strengthening is often used to discuss the strengthening mechanism induced by grain boundaries. Grain refinement strengthening is often described by the following Hall–Petch relation (Hall 1951; Petch 1953), formulated
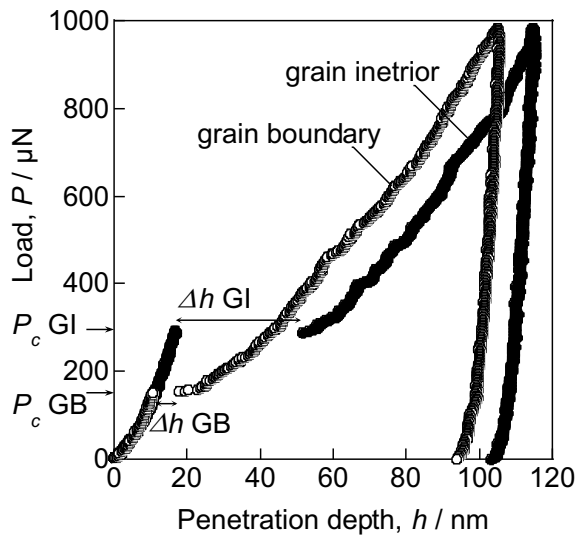
from the experimental results as

$$\sigma = \sigma_0 + kd^{-1/2}. \tag{8.5}$$

Here, σ refers to the flow stress σ_0 is a constant, k is the locking parameter, and d denotes the grain size. The pile-up model (Hall 1951; Petch 1953) and dislocation source model (Li 1963) are shown as the mechanisms for grain boundary strengthening. The former is understood as a function of resistance against dislocation motion, while the latter as a function of enhancing the dislocation generation, which seem to contradict each other at first glance. To verify these models, it is effective to directly capture the interaction between a single grain boundary and dislocation. However, in previous studies, only the microstructural observation by TEM (Hauser and Chalmers 1961; Carrington and McLean 1965; Shen et al. 1988; Kurzydlowski et al. 1984; Lee et al. 1990) has been conducted, and not the quantitative evaluation of the mechanical behavior. To address this problem, the authors performed nanoindentation in the vicinity of a single grain boundary and verified these two models from the viewpoint of mechanical behavior as described below.

The sample was Ti-added interstitial free (IF) steel, with an average grain size of several 100 μm. Details of the experimental method are shown elsewhere (Ohmura et al. 2005). The indented positions were set in two ways: just above the grain boundary and within the grain far from the grain boundary. Figure 8.4 shows an example of the load–displacement curves obtained from the nanoindentation measurements. The pop-in event clearly appeared on both the grain boundary (open circle) and grain interior (dot) on the loading curves. Figure 8.5 shows the relation between the critical load P_c and pop-in depth Δh. An example SPM image of the sample surface after the nanoindentation is inserted in the bottom right of the figure to

Fig. 8.4 Example of load–displacement curves obtained from nanoindentation measurements. Pop-in clearly appears on both the grain boundary (open circle) and grain interior (dot) on the loading curves (Ohmura et al. 2005). Reprinted with permission from [T. Ohmura, K. Tsuzaki and F. Yin: Mater. Trans., 46 (2005), 2026–2029.] Copyright (2005) by The Japan Institute of Metals and Materials
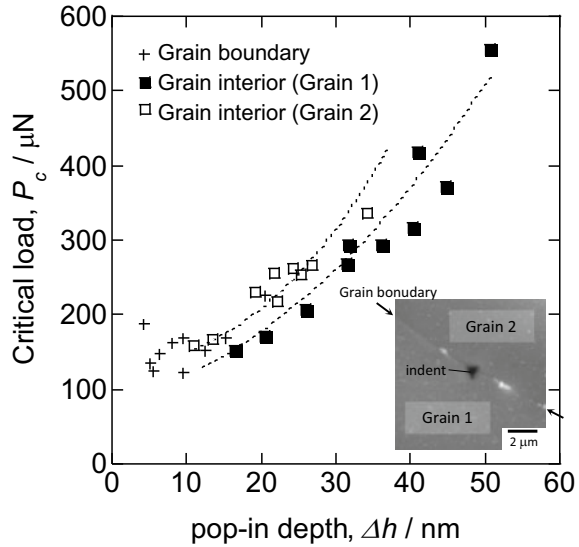
show that the indent mark is certainly formed just above the grain boundary. The two grains forming the grain boundary are named as grains 1 and 2, as shown in the figure, and the data of each grain's interior are plotted separately. On the grain boundary, P_c has relatively lower values of 100–200 μN, whereas in the grain interior, it is dispersed up to approximately 600 μN. The results suggest that grain boundaries act as effective dislocation sources for enhancing the dislocation emission for plasticity initiation. One of the characteristics of the grain interior data is that a higher P_c leads to a higher Δh. This can be understood in the following relation, derived from the model (Shibutani and Koyama 2004) in which plastic deformation upon the pop-in event is initiated by the prismatic loop dislocation generation (Ohmura et al. 2005):

$$P_c = \left(\frac{1}{0.18}\right)^3 \left(\frac{R}{E^*}\right)^2 \left(\frac{2G}{a}\Delta h + \mu\gamma\right)^3, \qquad (8.6)$$

where a indicates the horizontal size of the indent and γ denotes the elastic strain remaining after the pop-in. Equation (8.6), drawn by the broken line in the figure, fits well with the experimental data of the relation between P_c and Δh, and the higher the value of P_c, that is, the greater the accumulated elastic strain energy, the greater is the plastic strain at pop-in.

The reason why P_c is dispersed in the range of 100–600 μN is discussed below. The IF steel used in this experiment may have a higher dislocation source density before the indentation experiment as compared to the single-crystal sample shown in the previous section. When the initial dislocation source density is low, the indentation-induced stress at the pre-existing dislocation source does not reach the critical stress for dislocation source activation, and thus the plastic deformation must be initiated

through the generation of dislocations from the perfect crystal region. In contrast, when the dislocation source density is high, the plastic deformation starts with the activation of the pre-existing dislocation source without the nucleation of dislocation. The reason why P_c is distributed widely when the initial dislocation source density is high is, first, that the stress applied to the dislocation source varies depending on the position, because the stress field introduced by the indentation has a distribution. The maximum shear stress shown in Eq. (8.3) is the stress generated at a point just below the indenter, and it is rather rare that the position of the dislocation source coincides with that point and is further away from this point with a lower applied stress. Second, even if the dislocation source is located at the same position with the maximum shear stress, the critical stress required for the activation may depend on individual cases. Assuming, for example, a Frank Reed (FR) source as a dislocation source, the activating critical stress is *Gb/l* (*l* is the length of the FR source), where *l* may assume various values.

On the other hand, in the nanoindentation measurement, the hardness can be calculated from the indentation depth corresponding to the maximum load, as in the conventional method, and is determined as 2.8 ± 0.16 and 2.2 ± 0.05 GPa at the grain boundary and in the grain interior, respectively. The deformation resistance at the grain boundary is approximately 30% higher than that in the grain interior. This is interesting in contrast to the behavior described in Fig. 8.5, where the plastic deformation is initiated at the grain boundary at a lower stress than that in the grain interior. That is, while a single grain boundary initiates plastic deformation by acting as an effective dislocation source, when dislocation sources other than grain boundaries are activated in the further plastic deformation, the single grain boundary acts as a resistance against the sliding motion of dislocations moving toward the grain boundary, which indicates the remarkable contribution of the single grain boundary to strengthening in a certain strain region.

8.3.2 Solid Solution Element

Figure 8.6 shows typical load–displacement curves obtained by nanoindentation for Fe–C binary alloys with various carbon contents (Nakano and Ohmura 2020). In all loading processes, a displacement burst, indicated by dashed arrows, i.e., pop-in, occurred. As shown in Fig. 8.6, the critical load P_c at which pop-in occurs increases with the concentration of in-solution carbon.

Figure 8.7 shows the relation between the τ_{max} obtained by substituting the P_c value into Eq. (8.3), shown in Fig. 8.6, and the carbon concentration. The plots are averages and the error bars are standard deviations (SDs). As the carbon concentration increases, both τ_{max} and the SD increase.

To clarify the variation in the deviation, the probability distribution of P_c for each sample is shown in Fig. 8.8. The distribution of P_c is Gaussian-like at 0 C and 3 C, with a peak at around 350 µN. On the other hand, at a higher carbon concentration, the peak height around 350 µN decreases and another peak appears at the higher
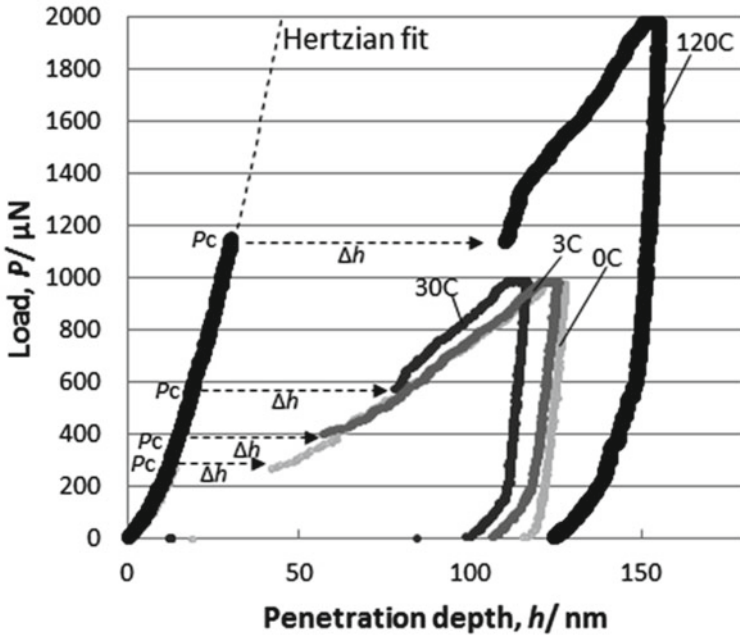
Fig. 8.6 Typical load–displacement curves for all samples (Nakano and Ohmura 2020).]. Reprinted with permission from [K. Nakano and T. Ohmura, J. Iron and Steel Inst. Japan, 106 (2020), 82–91.] Copyright (2020) The Iron and Steel Institute of Japan

Fig. 8.7 Relationship between solute carbon concentration and critical pop-in load Pc (Nakano and Ohmura 2020). Reprinted with permission from [K. Nakano and T. Ohmura, J. Iron and Steel Inst. Japan, 106 (2020), 82–91.] Copyright (2020) The Iron and Steel Institute of Japan
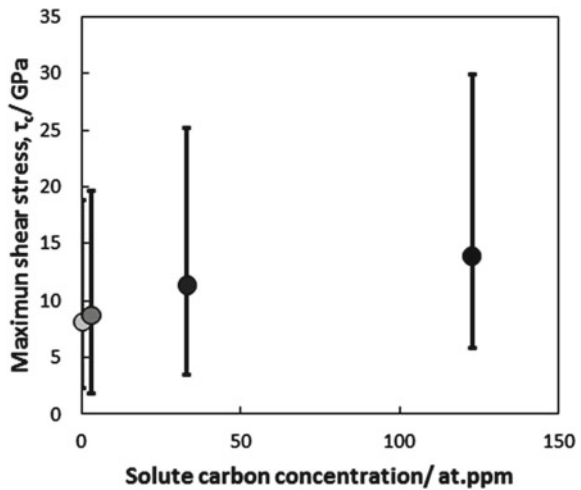
Fig. 8.8 Frequency of the critical pop-in load (Nakano and Ohmura 2020). Reprinted with permission from [K. Nakano and T. Ohmura, J. Iron and Steel Inst. Japan, 106 (2020), 82–91.] Copyright (2020) The Iron and Steel Institute of Japan
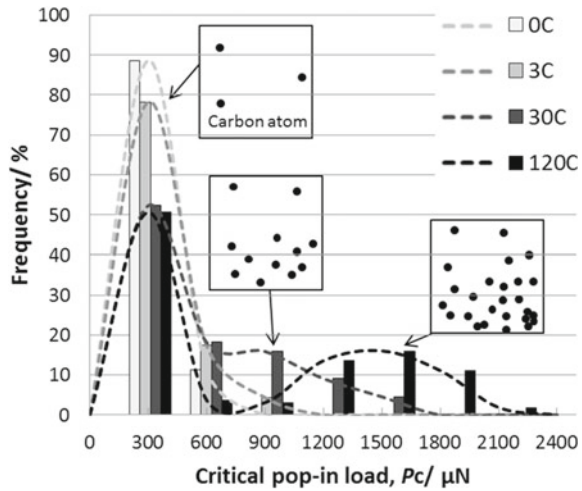
load over 500 μN. In addition, the peak position shifts to a higher load and the peak width widens for 120 C, compared to the case of 30 C. The pop-in phenomenon is controlled by the thermal activation process, because both peaks are Gaussian-distributed regardless of the position of the peak. Accordingly, the thermal activation process seems to be dominant for the pop-in generation, even if the solid-solution carbon atom is related.

The effect of solid-solution carbon on the pop-in phenomenon is discussed based on the mechanism of dislocation nucleation. The pop-in phenomenon corresponds to the onset of plastic deformation, as mentioned above. We previously (Zhang and Ohmura 2014) demonstrated experimentally that the pop-in phenomenon corresponds to the nucleation of dislocations from a defect-free region (see details in Sect. 8.4). Lorentz et al. (2003) concluded that dislocation generation is a homogeneous nucleation of the shear dislocation loop, because the experimentally measured shear stress at pop-in agrees well with the ideal strength. On the other hand, Schuh et al. (2005) found the activation volume from the probability distribution function of the pop-in stress and indicated that the inhomogeneous nucleation dominates the event because the activation volume is very small below 1.0 b^3 (b is the magnitude of Burgers vector). As the occurrence of the shear dislocation loop is considered an elementary process in both cases, Sato et al. (2019) modeled this process using the molecular dynamic simulation at finite temperature and showed that the temperature dependence of τ_{max} agreed well with the experimental results of W and Fe. Thus, experiments and atomic simulations show that dislocation nucleation is necessary for pop-in formation, and the thermal activation process is considered dominant even in the presence of solid-solution carbon atoms. Thus, these carbon atoms increase τ_{max} to resist this nucleation process. A detailed model of this mechanism is described later.

The reason why the frequency distribution of P_c varies with the carbon concentration is discussed subsequently. As shown in Fig. 8.8, as the carbon concentration increases, the peak around 350 μN remains constant, while the other peak position shifts to a higher load. This trend suggests a nonuniform carbon distribution. The peak at 350 μN corresponds to the behavior under the carbon-free condition because the peak appears even in the 0 C sample. If the spatial distribution of carbon atoms remains uniform after the in-solution carbon concentration increases, only the average value is expected to increase while the distribution shape remains a single peak. Therefore, the multiple peaks suggest that different mechanisms dominate the pop-in behavior. As the peak position at 350 μN is constant regardless of the carbon concentration and the peak is highest in the 0 C sample, the mechanism is governed by the same resistance to dislocation nucleation, where in-solution carbon atoms are hardly involved. On the other hand, the peak at the higher load positions that appears after the carbon addition is considered to be caused by the interaction between single or multiple in-solution carbon atoms and dislocations with higher resistance to dislocation nucleation. The reason why the peak position shifts to the high load side with an increase in the carbon concentration is attributed to the shortening of the distance between the carbon atoms in solution. These are considered from the dislocation nucleation model developed by Sato et al. (2019), as follows. Assuming that the elementary process of the pop-in phenomenon is the nucleation of the shear dislocation loop, the applied force is balanced with a line-tension force under the condition of a loop curvature smaller than the critical size. Therefore, when the diameter of the shear dislocation loop is smaller than the critical size, the loop disappears upon unloading. To reach and overcome the critical size for a stable growth of shear dislocation loops, it is necessary to further increase the applied force or weaken the line tension through thermal fluctuation. That is, it is necessary to exceed the critical size of the dislocation loop in order for the dislocation to nucleate and pop-in to occur. Under a certain external force, dislocation loops of various sizes are generated by the thermal activation process, while those below the critical size disappear. The higher the applied stress, the lower is the activation energy required for dislocation nucleation and the smaller is the critical radius. The above model indicates that a higher stress is required at the same temperature to reach the critical size under the effect of in-solution carbon atoms, because carbon atoms generate resistance to the growth of dislocation loops by pinning the migration of dislocation lines. Therefore, the peak of the higher load side, which appears when the carbon concentration increases, appears because single or multiple solid-solution carbon atoms act as a large resistance to dislocation motion. As the solid-solution carbon concentration increases, the distance between the in-solution carbon atoms decreases and some atoms may form a cluster (Ushioda et al. 2019). It is considered that the peak position shifts to the higher load side with an increase in the carbon concentration, cluster number density, and cluster size.

The reason why the distribution width on the high load side increases with the carbon concentration needs to be discussed. This is synonymous with the increase in the error bar shown in Fig. 8.7 and is considered to be an essential result of the distribution of in-solution carbon atoms rather than the measurement error. When

the carbon concentration increases, the average distance between the carbon atoms decreases and the formation frequency of the local aggregates, such as a cluster, increases. There are various cluster sizes under this condition, and the spatial distribution of number density arises. The reason why the distribution width of the high load side expands is attributed to the fact that the distribution of number density and cluster size increases with the carbon concentration. On the other hand, the distribution width on the low load side does not change even when the carbon concentration increases. As described above, this peak is attributed to the mechanism in which carbon atoms are not involved, and therefore there might be a region in which carbon atoms do not exist depending on the measurement position, even if the sample includes nominal carbon atoms. The volume of this region is expected to be more than that of the plastic region formed underneath the indenter. It is reported that the diameter is approximately 10 times the indentation depth when the plastic region under the indenter is assumed to be hemispherical (Itokazu and Murakami 1993). As the indentation depth corresponding to the peak on the low load side is 10–20 nm, the corresponding diameter of the plastic region is estimated to be 0.1–0.2 μN. That is, the region with no carbon atoms is estimated to be larger than this size, and this region is considered to be randomly dispersed in the sample. Based on the model, as shown in the schematic diagram in Fig. 8.8, as the nominal carbon concentration increases, the local concentration increases in the region where solid-solution carbon atoms exist, while there are regions where almost no atoms exist, which leads to a significant inhomogeneity in the distribution of these atoms.

8.3.3 Initial Dislocation Density

Pre-existing lattice defects, including dislocations, affect the behavior of plasticity initiation underneath an indenter. The STEM micrographs for ultra-low carbon (ULC) and IF steels with different dislocation densities are shown in Fig. 8.9 (Sekido et al. 2012). The recrystallized samples are tensile-deformed up to approximately 40% strain at room temperature to get a high dislocation density of 10^{14} m^{-2}. For the other specimens, the recrystallized samples are further annealed at 1123 K for 7.2 ks, and then held at 973 K for 1.8 ks, followed by cooling to room temperature in air, obtaining a low dislocation density of 10^{11} m^{-2}. Figure 8.10 shows typical load–displacement curves for (a) the specimens after tensile deformation and (b) the full-annealed one in both ULC and IF steels. Pop-in phenomenon appears clearly in the low-dislocation-density steels in Fig. 8.10a, and the critical load for the pop-in in ULC is higher than that in the IF. On the other hand, no clear pop-in is observed in steels with high dislocation density shown in Fig. 8.10b. Even though the pop-in phenomenon is not clear in Fig. 8.10b, the critical pop-in load P_c can be found using the Hertz contact curve of Eq. (8.1) by a deviation from the broken line. Compared to Fig. 8.10a, b, the P_c values are extremely low and the effect of solid-solution elements is unclear in (b), with a higher dislocation density. Figure 8.11 a–d shows the plots of P_c versus Δh for IF and ULC with low and high dislocation densities. The following
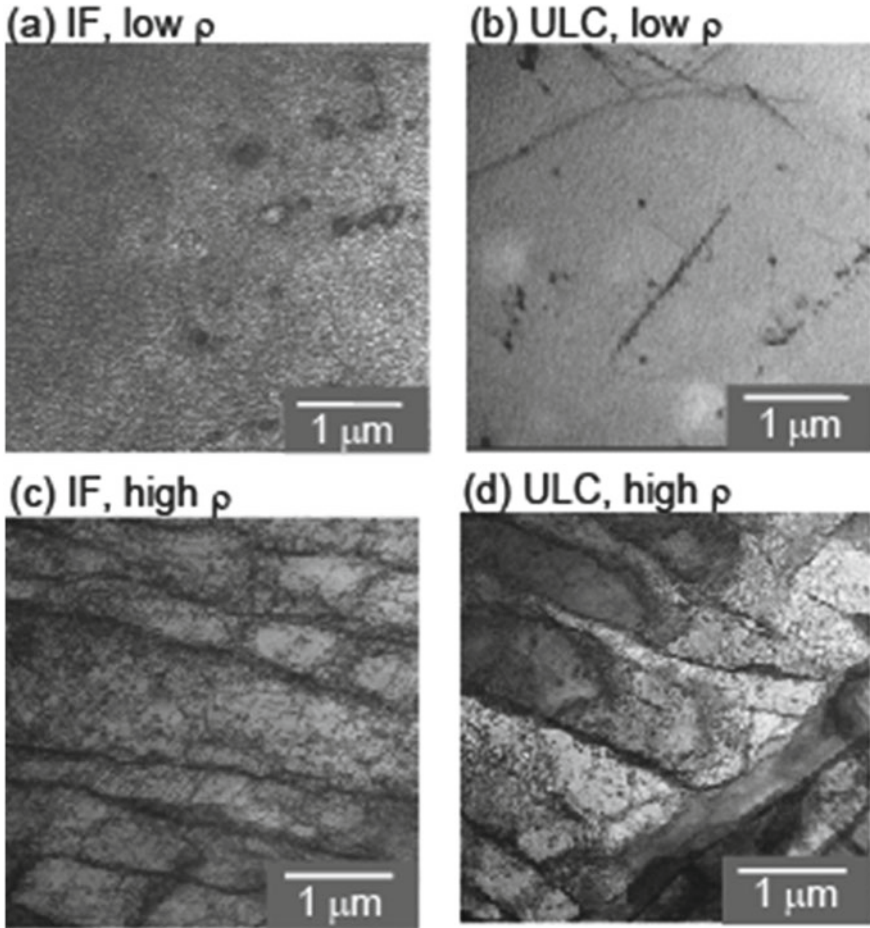
Fig. 8.9 STEM images for IF and ULC with **a**, **b** low dislocation density and **c**, **d** high dislocation density (Sekido et al. 2012). Reprinted with permission from [K. Sekido, T. Ohmura, T. Hara and K. Tsuzaki: Mater. Trans., 53 (2012), 907–912.] Copyright (2012) by The Japan Institute of Metals and Materials

three points can be gotten from the figures. First, the average P_c in the ULC steel is higher than that in the IF steel with low dislocation density. Second, the average P_c in the high-dislocation-density samples is lower than that in the low-dislocation-density materials. Third, the average P_c in the ULC steel is almost the same as that in the IF steel with high dislocation density. Leipner et al. (2001) described the critical stress τ_n for the dislocation nucleation in GaAs under indentation-induced stress field. The equation is given as

$$\tau_n = \frac{Gb}{\pi e^3 r_0} \frac{2 - \nu}{1 - \nu}, \tag{8.7}$$

Fig. 8.10 Typical load–displacement curves for IF and ULC with **a** low dislocation density and **b** high dislocation density (Sekido et al. 2012). Reprinted with permission from [K. Sekido, T. Ohmura, T. Hara and K. Tsuzaki: Mater. Trans., 53 (2012), 907–912.] Copyright (2012) by The Japan Institute of Metals and Materials
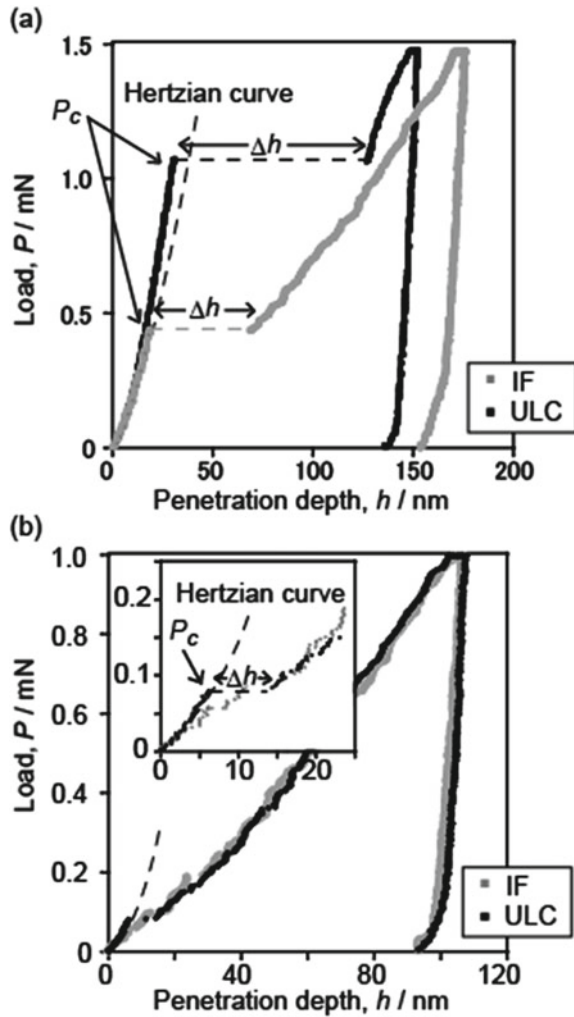
where e is the Euler number and r_0 is the cutoff radius at the dislocation core. We obtain $\tau_n \approx 9.7$ GPa using the typical values of $r_0 = b/3$, $b = 0.29$ nm, $G = 83$ GPa, and $\nu = 0.3$ for ferrite. Meanwhile, the maximum shear stress τ_{max} underneath the indenter can also be determined from Eq. (8.3) to be approximately 13 and 18.5 GPa for IF and ULC steels, respectively. In the high-dislocation-density materials, τ_{max} is lower than τ_n, suggesting that the plasticity initiation is dominated by not dislocation nucleation but another mechanism with a lower critical stress. In high-dislocation-density materials, the microstructure can include numerous dislocation sources that have been generated by lattice defects reactions during the tensile deformation, and some dislocation sources may be activated at a lower applied stress than the critical shear stress τ_c for the indentation-induced dislocation source, and/or pre-existing
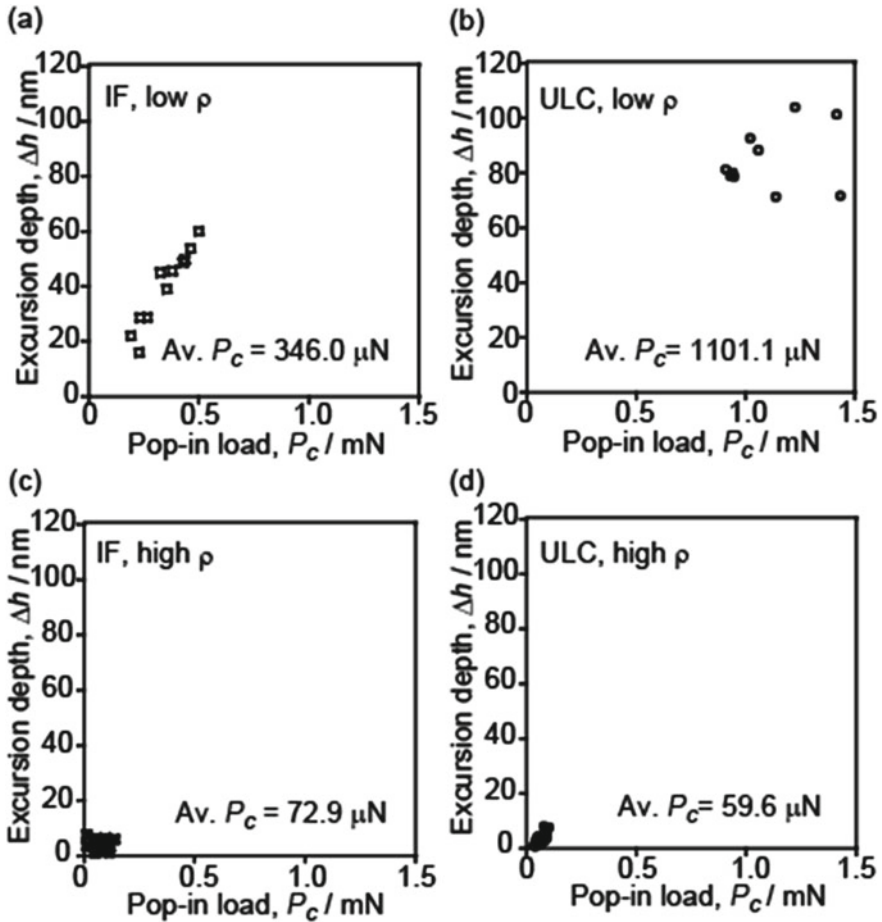
Fig. 8.11 Relationship between P_c and Dh for IF and ULC with **a, b** low dislocation density and **c, d** high dislocation density (Sekido et al. 2012). Reprinted with permission from [K. Sekido, T. Ohmura, T. Hara and K. Tsuzaki: Mater. Trans., 53 (2012), 907–912.] Copyright (2012) by The Japan Institute of Metals and Materials

dislocations may start to move at a lower stress than that of dislocation nucleation. Accordingly, the plasticity initiation under an indentation-induced applied stress is presumably dominated by the multiplication and/or inception of glide motion of a pre-existing dislocation underneath the indenter. Consequently, the plastic deformation is initiated at a lower load.

There is no significant difference in P_c between the IF steel in Fig. 8.11c and the ULC steel in Fig. 8.11d, indicating that interstitial carbon has no effect on the pop-in event in high-dislocation-density materials. The thermal activation process of the dislocation motion is discussed subsequently to determine the effect of interstitial carbon on the pop-in event on an experimental approach. The passing mechanism of

dislocation on the interstitial carbon should be a thermal activation process because interstitial carbon is a short-range obstacle for dislocation glide motion. Therefore, the pop-in behavior could be affected by the interstitial carbon in ULC steel, and P_c should show an indentation rate dependence (Sekido et al. 2011a). Figure 8.12a, b shows the loading rate dependence of P_c with low- and high-dislocation-density materials, respectively. In low-dislocation-density materials, the P_c in ULC steel shows a clear indentation rate dependence, while in high-dislocation-density materials, no dependence is shown in IF and ULC steels. These results indicate that there

Fig. 8.12 Indentation rate dependence for IF and ULC with **a** low dislocation density and **b** high dislocation density (Sekido et al. 2012). Reprinted with permission from [K. Sekido, T. Ohmura, T. Hara and K. Tsuzaki: Mater. Trans., 53 (2012), 907–912.] Copyright (2012) by The Japan Institute of Metals and Materials
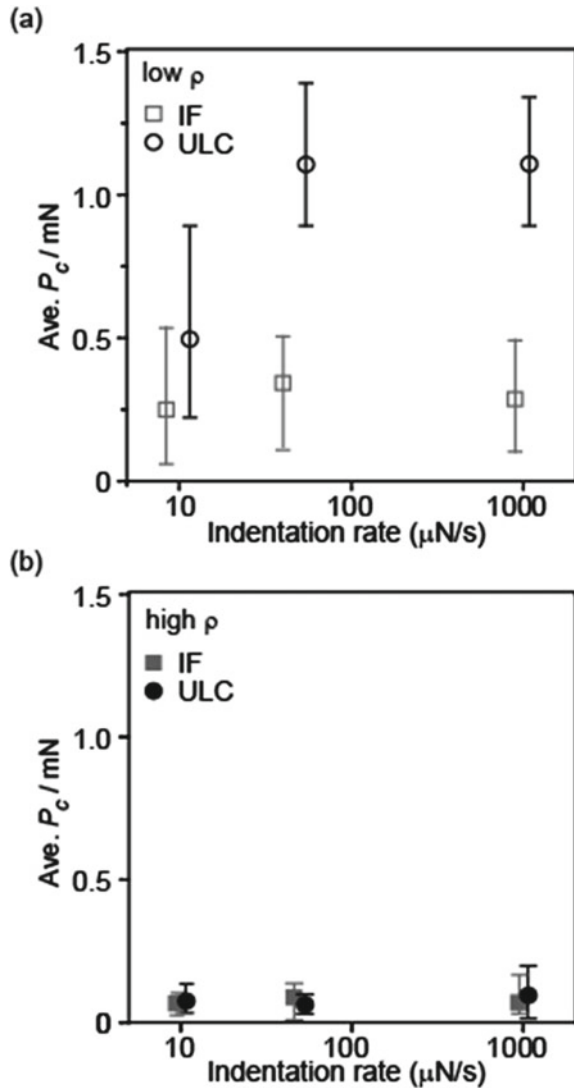
is no effect of interstitial carbon on the pop-in event of the plasticity initiation for high-dislocation-density materials.

Next, we discuss two reasons why carbon does not have any effect on the ULC with high dislocation density under the occurrence of dislocation multiplication.

The first reason is that the dislocation with no carbon pinning could be the dominating mechanism. Britton et al. (2009) discussed the relation between the amount of carbon and the dislocation density for a pop-in event, using the Fe—0.01 wt%C polycrystal (bcc) based on Cottrell and Bilby's model (1949). This model explains the effect of carbon content, ω (wt%), on the stress–strain curve of steels with different dislocation densities ρ (m^{-2}). A yield drop occurs on the stress–strain curve when

$$\omega/\rho \geq 10^{-18} (\text{wt\%m}^2). \tag{8.8}$$

In contrast, no yield drop appears when

$$\omega/\rho \geq 10^{-19} (\text{wt\%m}^2). \tag{8.9}$$

Thus, they concluded that pop-ins do not occur in the sample with many dislocations, as there are not enough carbon atoms to pin all dislocations, which is analogous to the case of the ULC with high dislocation density in our study. In the ULC steel, the carbon content is 0.0038 wt%, and dislocation densities are 10^{11} m^{-2} and 10^{14} m^{-2} for lower and higher samples, respectively. ω/ρ is estimated to be 10^{-14}(wt%m^2) for the low dislocation density, which satisfies Eq. (8.8), resulting in an occurrence of pop-in. On the other hand, ω/ρ is calculated as 10^{-17}(wt%m^2) for high-dislocation-density sample, which is two orders higher with the critical value in Eq. (8.9). However, the carbon content can be overestimated in the grain interior because the carbon atoms tend to segregate to the grain boundaries and therefore the actual carbon content in the grain interior can be lower than the nominal value in the whole sample. Additionally, the dislocation density can be underestimated as we can measure it only in the interior of the dislocation cells and cannot count the dislocations on the cell walls. Therefore, the real value of ω/ρ can be much lower than the estimated, corresponding to the case of Eq. (8.9). Consequently, we can presume that a part of the pre-existing dislocations is free from pinning by carbon and can move in the same manner as the dislocations in the IF as many pre-existing dislocation and sources exist underneath the indenter.

The other reason is that the critical stress required for dislocation source activation is more dominant than unpinning from carbon. We estimate the balance between the carbon contents and the dislocation density for the ULC steel with high dislocation density. In this estimation, all carbon atoms are assumed to exist in the grain interior with no segregation or precipitation. The number of carbon atoms per unit volume, N^c_v, in the ULC steel that is estimated from the carbon composition is as follows. The carbon content in the ULC is 0.0177 at%; thus, the average spacing of carbon is estimated to be approximately 4 nm, and N^c_v is calculated to be 1.6×10^{25} m^{-3}. On the other hand, the number of carbon atoms segregating on a dislocation, N^d_v, is calculated from the dislocation density. We assume the spacing of the carbon to be

0.29 nm, which is the nearest neighbor of the octahedral site. $N^d{}_v$ is obtained as the dislocation density (10^{14} m^{-2}) divided by the spacing of carbon atoms (0.29 nm) to be 3.4×10^{23} m^{-3}. Based on the estimations, $N^c{}_v$ is much larger than $N^d{}_v$, indicating that the carbon content is high enough to pin all dislocations. Thus, another possibility should be considered. On the other hand, in the line-tension model of dislocation, the critical stress τ_p required for the dislocation multiplication from FR-type source is expressed as

$$\tau_p = \frac{Gb}{l_p}, \tag{8.10}$$

where l_p is a FR length. τ_p is dominant if it is greater than the stress required for unpinning from the carbon. Even though it is not easy to estimate the stress required for unpinning from the carbon in an individual dislocation, the yield stress given by the tensile test is approximately 300 MPa (Sekido et al. 2011a); hence, a high probability is given for dislocation glide motion at this stress level for getting a certain plastic strain in the initiation of deformation. On the other hand, the τ_{max} calculated from P_c in Eq. (8.3) is approximately 8 GPa. Since there is a stress distribution underneath the indenter and the position of the activated dislocation source can be far from the position of τ_{max}, the actual τ_p might be lower than 8 GPa. However, the τ_p value can still be much higher than the macro-yield stress level. Thus, the critical stress τ_p for the activation of the pre-existing dislocation and dislocation source that is induced by tensile deformation is dominant for the pop-in event and unpinning from the carbon has no effect on the ULC with high dislocation density. In this case, P_c is associated with the τ_p in Eq. (8.10); hence, in-solution carbon is not related to P_c. This result is similar to the low-average P_c at grain boundaries, indicating that the presence of the dislocation source is related to the initiation behavior of plastic deformation.

8.4 Initiation and Subsequent Behavior of Plastic Deformation

8.4.1 Sample Size Effect and Elementary Process

One factor that determines the critical stress τ_y for the onset of plastic deformation on a slip plane is the Peierls potential, which changes the self-energy of dislocations due to the periodicity of the crystal structure. The parameter τ_y indicates the stress required to cross one of the peaks of the Peierls potential (Peierls stress) without thermal assistance. It has been shown experimentally for various materials that τ_y is expressed in the following form by using the shear modulus G, the spacing between lattice planes h, and the magnitude of Burgers vector b (Takeuchi and Suzuki 1989;

Suzuki and Takeuchi 1989).

$$\tau_y = \alpha G \exp\left(-\beta \frac{h}{b}\right), \tag{8.11}$$

where α and β are constants. As τ_y is normalized by G and τ_y/G depends only on the value of h/b, the critical shear stress is almost determined by the crystal structure and lattice constant. As described above, in the case of a high-purity crystal, especially a crystalline material other than a metal and low-temperature deformation of bcc metal, the yield stress is determined by the intrinsic factor of the crystal for dislocation glide motion.

The above interpretation is a model for understanding the macroscopic yield phenomenon of a single crystal by the motion of a single dislocation. In other words, the model assumes that a mobile dislocation already exists in the crystal and that its motion governs the plasticity.

This raises one question. Where does the mobile dislocation originate in the crystal before yielding? Is it the so-called grown-in dislocation, or is it a dislocation formed or grown during deformation?

The high strength of the whisker was originally attributed to its defect-free nature, but it is understood that the strength strongly depends on the sample size and that the thinner the crystal, the lesser is the probability that a longer dislocation source exists in the sample (Brenner 1956). More recently, Uchic et al. (2004), in a systematic study of cylindrical single-crystal samples of sizes ranging from 0.5 to several 10 μm, showed that the yield stress measured in compression tests increased with the decreasing cylinder diameter. The reason for this is attributed to the fact that the smaller the sample size, the lower is the number of initial mobile dislocations involved. Note that the yield stress depends on the sample size, that is, the critical shear stress of a slip plane depends on the number of dislocations or the number of dislocation sources included in the stress field. This may provide a new insight into the strengthening mechanism in grain refinement strengthening, for example. The conventional mechanism model of grain refinement strengthening is grain boundary strengthening, which is an obstacle to the glide motion of dislocations at grain boundaries as an elementary process. Besides the conventional model, it is also necessary to consider that the yield stress in the grain interior increases due to the grain size effect. The authors demonstrated that the hardness of the grain interior, as well as the macro-hardness for ultrafine-grained materials of IF steel and pure Al, increases according to the grain size (Ohmura et al. 2004a; Zhang et al. 2009). The fact that the yield stress in the grain interior depends on the grain size indicates that the σ_0 term in Eq. (8.5), which has been considered to be the material constant regardless of the grain size, does not have a constant value and contains important suggestions concerning the strengthening mechanism.

Another important point in the dependence of strength on the sample size is that not only the mobile dislocation density but also the dislocation source density is related to the mechanical behavior. In dislocation theory, when the dislocation density ρ at

a certain instant is constant, the strain rate $\dot{\gamma}$ is expressed by a model governed by the average mobility of dislocations $\overline{v}$ and b, as follows:

$$\dot{\gamma} = \rho b \, \overline{v}. \tag{8.12}$$

This model is useful for explaining the thermal activation process of deformation based on the temperature dependence of the dislocation mobility by the finite velocity caused by viscous motion. In the discussion of the macroscopic plastic strain, a statistical mechanical approach is possible because it can be regarded as the average velocity of many dislocations or that of one dislocation during its long-range motion. The analysis of the general thermal activation process is often based on this model.

On the other hand, in the case of flight motion in which the generated or grown dislocations move at a constant distance instantaneously, the strain rate $\dot{\gamma}$ is given by

$$\dot{\gamma} = \dot{\rho} b \bar{x}, \tag{8.13}$$

where $\dot{\rho}$ is the increase rate of dislocation density and $\overline{x}$ is the average travel distance of the dislocation glide motion. In this case, $\overline{x}$ is considered to be the distance to a mechanical equilibrium position or to the surface, which can be considered constant in a short time. Therefore, the strain rate is controlled by the growth rate of dislocations $\dot{\rho}$ at a moment. This model seems to be close to reality as an elementary process of plastic deformation, if the material deformation is modeled locally and/or from the short time viewpoint. In fact, as clearly observed in Fig. 8.2, the dislocation density rapidly increases in a very short time and the generated dislocation immediately moves a certain distance. For the bulk material, the following results are obtained on the dislocation structure introduced upon pop-in Zhang and Ohmura (2014). Figure 8.13 shows (a) the SPM image of indentation marks on the sample surface, (b) the corresponding load–displacement curves, and (c) the cross-sectional TEM images of the dislocation structure just below the indent marks. As shown in (a), even though the same peak load is applied to 3 × 8 regularly arrayed positions, no indentation is formed in some cases. For example, the load–displacement curves of 1–3 in (b) correspond to their indent marks in the bottom row on the SPM image in (a). In case of indent 2, no indentation is formed in (a), and the load–displacement curve in (b) shows a complete elastic deformation in which the loading and unloading curves overlap, and no dislocation is observed in the TEM image in (c). On the other hand, in case of indent 3, the unloading starts immediately after pop-in according to the load–displacement behavior in (b), and therefore almost all dislocations observed in (c) are introduced at the moment of pop-in. Compared to case 1, in which certain plastic deformation progresses after pop-in, dislocation structures in cases 1 and 3 are not much different in terms of distribution range and many complicated dislocation lines. A comparison of these three cases indicates that several dislocations are generated at the instant of pop-in and move to a certain distance, and then the deformation progresses while the dislocation structure develops gradually in the subsequent deformation. That is, the growth-dominated deformation of Eq. (8.13) progresses at the
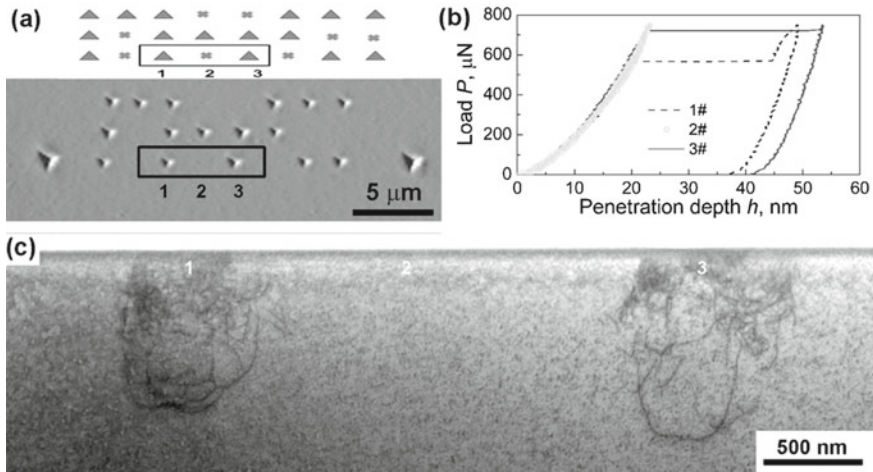
Fig. 8.13 a SPM image of indentation marks on the sample surface, **b** the corresponding load–displacement curves, and **c** the cross-sectional TEM images of the dislocation structure just below the indent marks (Zhang and Ohmura 2014). Reprinted with permission from [L. Zhang and T. Ohmura: Phys. Rev. Lett., 112 (2014), 145,504.] Copyright (2014) by The American Physical Society

instant of pop-in, and thereafter the mobility-dominated deformation of Eq. (8.12) progresses.

Although the relation between the two models is controversial, both are very important in discussing the mechanism of plastic deformation. As it was conventionally difficult to capture individual dislocation motions directly, an average handling had to be conducted. The model expressed in Eq. (8.12) is suitable for discussing the macroscopic behavior. On the other hand, the recent advanced observation and analysis technologies, including TEM in situ straining, have made it possible to approach the behavior on the scales of micron or less, as well as more precise elementary process analysis (Ohmura et al. 2004b; Zhang et al. 2011; Carpeno et al. 2015; Hsieh et al. 2016; Chung et al. 2018; Onose et al. 2019; Kim et al. 2012). It is necessary to verify how the conventional knowledge matches the new knowledge by the advanced research approach or whether it does not match without sticking to the complexes.

8.4.2 Dislocation Mobility and Mechanical Behavior in Bcc Crystal Structures

Note that the 1/2 <111> screw dislocations in bcc crystals exhibit a large Peierls force due to the specificity of the atomic arrangement and dislocation core structure (Hirsch 1968; Vitek 1974; Suzuki 1968; Takeuchi 1981; Edagawa et al. 1997), and they are considered to have significantly lower mobility than edge dislocations. It has been

experimentally observed that linear screw dislocations are dominant in dislocation structures after deformation in bcc single crystals. This behavior is understood as the reason for the anomalous properties in that the yield stress of bcc crystals is higher than that of fcc crystals in the low-temperature range, the temperature dependence of the yield stress is large, and CRSS shows plastic anisotropy depending on the shear direction (failure of Schmid's law).

In general, the relation between dislocation mobility and applied stress is expressed by the following equation, as dealt with in Johnston–Gilman's theory (Johnston and Gillman 1959; Johnston 1962):

$$\overline{v} \propto \tau^m. \tag{8.14}$$

The stress exponent m varies depending on the crystal and is relatively small in the case of a semiconductor or an ionic crystal and large in the case of a metal. From Eqs. (8.12) and (8.14), the relation between strain rate $\dot{\gamma}$ and applied stress τ is expressed as follows:

$$\dot{\gamma} \propto \rho b \tau^m. \tag{8.15}$$

Therefore, under the condition that m is small, the strain rate dependence of the applied stress increases and the mobility of the dislocation dominates the yield stress. Based on this model, the reasons why the temperature dependence of the yield stress of bcc crystals is high can be understood by the low mobility of screw dislocations.

The relation between the dislocation mobility and applied stress is directly observed by TEM in situ micropillar compression deformation analysis using the Fe alloy single crystal (Zhang et al. 2012). Figure 8.14a, b shows snapshots extracted from movies of deformation during the tests. Figure 8.14c shows the load–displacement data recorded in synchronism with the observation, as well as the relation between the dislocation behavior and mechanical response. The compression axis of the pillar is parallel to the <110> axis, and the directions in which the two <111> directions that can be potential. Burgers vectors are indicated by arrows in Fig. 8.14a, b. The dislocation component is roughly judged from the relation between a line vector of the dislocation and the direction of the Burgers vector <111> . The screw component dominates when the dislocation line is parallel to the compression axis of the pillar, while the edge dislocation dominates the perpendicular dislocation line. In the dislocation shown in Fig. 8.14a, the edge component is judged to be dominant from the direction of the dislocation line. The two images (a1) and (a2) shown in Fig. 8.14a are taken at 1/30 s intervals. During the interval, the edge dislocation moves instantaneously from the left end to the right end in the figure, indicating a very high movement speed. The moment this phenomenon is observed, the corresponding mechanical behavior is indicated by arrow 1 on the load–displacement curve, which is the first half of the relatively lower stress deformation. On the other hand, in the dislocation shown in (b), as the dislocation line is almost parallel to the <111> axis, it can be judged that the screw component is dominant. Comparing (b2) and (b1) recorded at intervals of approximately 3 s, to examine the moving speed,
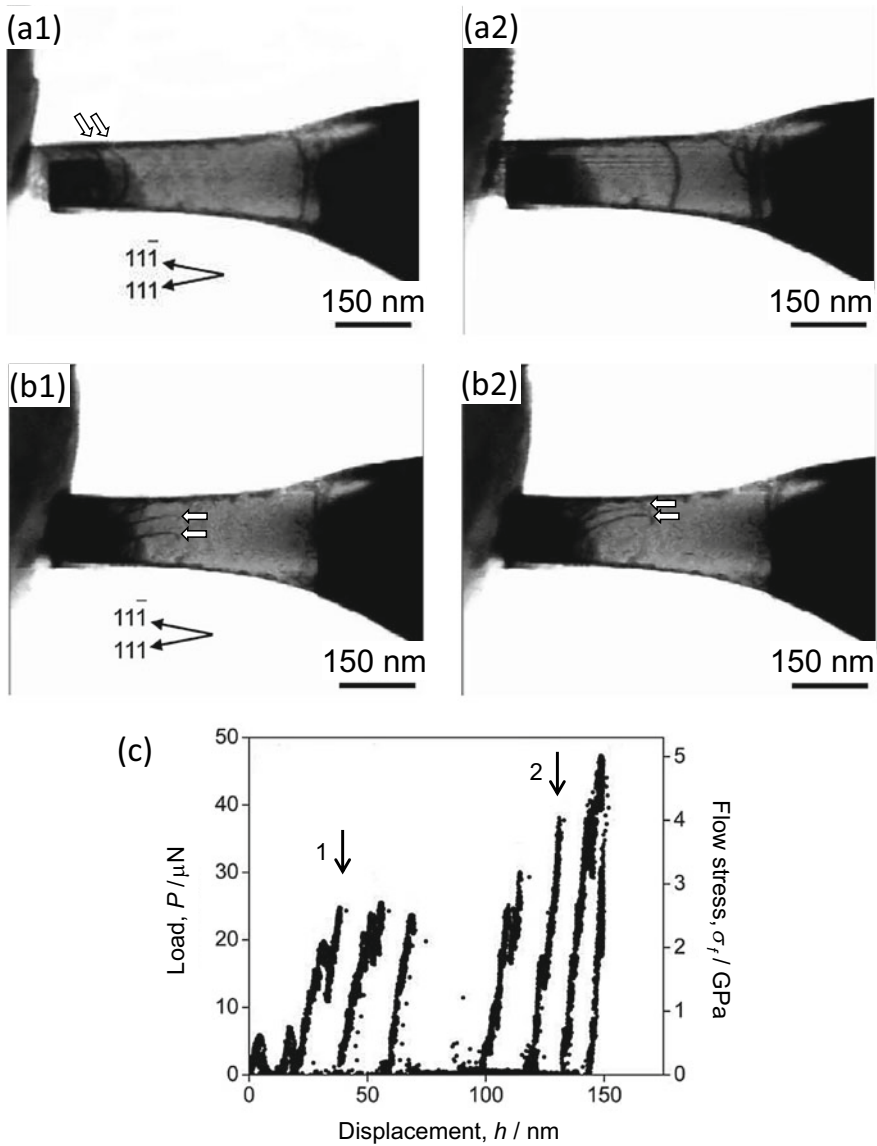
Fig. 8.14 a and **b** are snapshots extracted from movies of deformation during the tests. Figure 8.10c shows the load–displacement data recorded in synchronism with the observation (Zhang et al. 2012). Reprinted with permission from [L. Zhang, T. Ohmura, K. Sekido, T. Hara, K. Nakajima and K. Tsuzaki: Scripta Mater., 67 (2012), 388–391.] Copyright (2012) by Elsevier

while the time intervals are nearly 10 times as long as those of (a1) and (a2), the travel distance during the time interval is small and the moving speed is much lower than the edge dislocation. The mechanical behavior corresponding to the moment with screw dislocation dominancy is the position on the load–displacement curve, indicated by arrow 2 in (c), and the flow stress is higher than that in the case of edge dislocation in (a). These results indicate that the mobility of screw dislocations in bcc metals is extremely lower than that of edge dislocations, and the flow stress is thereby increased.

In addition, the TEM in situ deformation analysis of IF steel successfully captures the dynamic relation between dislocation density and flow stress under the condition dominated by screw dislocations (Zhang et al. 2014). The sample exhibits a blade-like shape with a height and width of approximately 600 nm and a thickness of approximately 80 nm. Figure 8.15a shows the true stress–true strain curves measured simultaneously with TEM observation with two curves to show reproducibility. Figure 8.15b–f shows snapshots taken from a movie recorded by TEM in situ deformation. The compression axis is horizontal, and a diamond flat-end punch approaches the specimen from the left side of the figure. As shown in Fig. 8.15b, the dislocation density before the yield stress is extremely low. The yield stress obtained from (a) exceeds 1.0 GPa, which is orders of magnitude higher than the bulk yield stress. This is consistent with the size-dependent behavior described in Sect. 8.4.
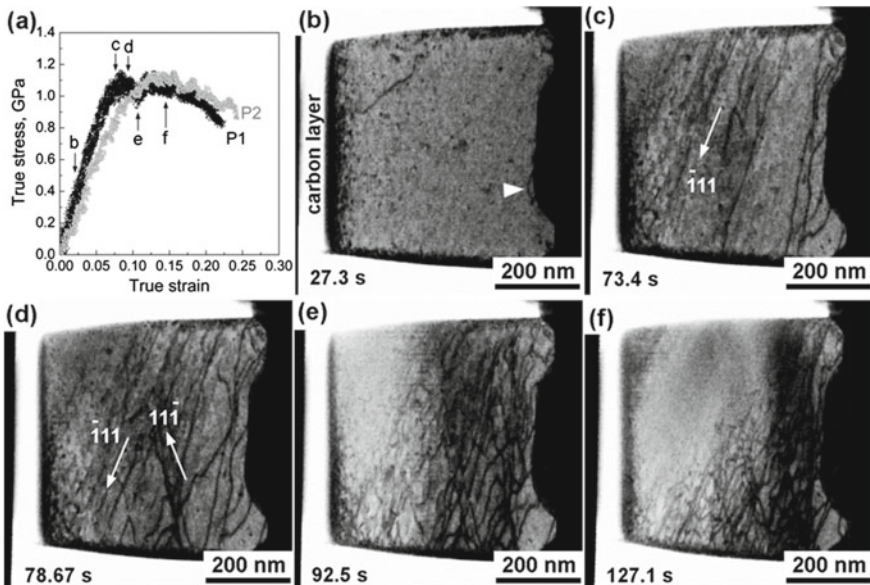
Fig. 8.15 a True stress—true strain curves measured simultaneously with TEM observation. **b–f** are snapshots taken from a movie recorded by TEM in situ deformation (Zhang et al. 2014). Reprinted with permission from [L. Zhang, N. Sekido and T. Ohmura: Mater. Sci. Eng., **A611** (2014), 188–193.] Copyright (2014) by Elsevier

Fig. 8.16 Results of fitting
by Eq. (8.16) for changes in
flow stress obtained from the
stress–strain curve and
dislocation density obtained
from TEM images (Zhang
et al. 2014). Reprinted with
permission from [L. Zhang,
N. Sekido and T. Ohmura:
Mater. Sci. Eng., A611
(2014), 188–193.] Copyright
(2014) by Elsevier
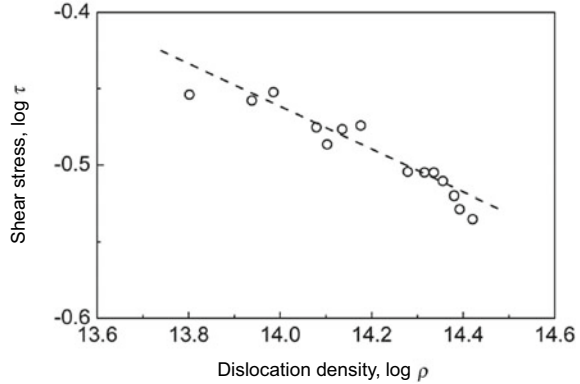
After yielding, the stress tends to decrease gradually. At the same time, the dislo-
cation density is observed to increase gradually. The relation between flow stress
and dislocation density is discussed below. In this case, unlike the case of Fig. 8.2,
the increase in dislocation density is slow, and thus the number of dislocations for
a short time can be regarded as constant. The deformation is under the dislocation
mobility, not under the growth of dislocation density, and the relation between the
macroscopic plastic strain rate and dislocation density is discussed using Eq. (8.12).
As the relation between the dislocation mobility and the applied stress is given by
Eq. (8.14), under the condition that the moving speed of dislocations, which give
plastic deformation, is the same, the relation between the shear stress and dislocation
density is arranged as follows:

$$\log \tau \propto A - \frac{1}{m} \log \rho, \tag{8.16}$$

where A is a constant. Figure 8.16 shows the results of fitting by Eq. (8.16) for the
changes in flow stress obtained from the stress–strain curve and dislocation density
obtained from TEM images. From this plot, the exponent m value is determined to
be approximately 7. According to the literature (Stein and Low 1960), the m value
obtained from experimentally determining the relation between shear stress and the
mobility in an edge dislocation dominancy in Fe-Si alloy is approximately 40, which
is 6 times larger than the result shown in Fig. 8.16. This is attributed to the fact that the
mobility of screw dislocations in bcc is lower than that of edge dislocations, which is
consistent with our understanding of the mobility of screw dislocations. Additionally,
the values of the stress exponent m are discussed as follows. In Eq. (8.15), under the
condition that the dislocation density is constant, the relation between the strain rate
and stress can be expressed as follows:

$$\frac{\partial \ln \dot{\gamma}}{\partial \tau} = \frac{m}{\tau}. \tag{8.17}$$

Fig. 8.17 Results of the
yield stress of pure iron
single crystal and its strain
rate dependence (Aono et al.
1981). Reprinted with
permission from [Y. Aono,
E. Kuramoto and K.
Kitajima: Rep. Res. Inst.
Appl. Mechanics, Kyu-shu
Univ. XXIX, (1981), 127.]
Copyright (1981) by
Research Institute for
Applied Mechanics, Kyushu
University
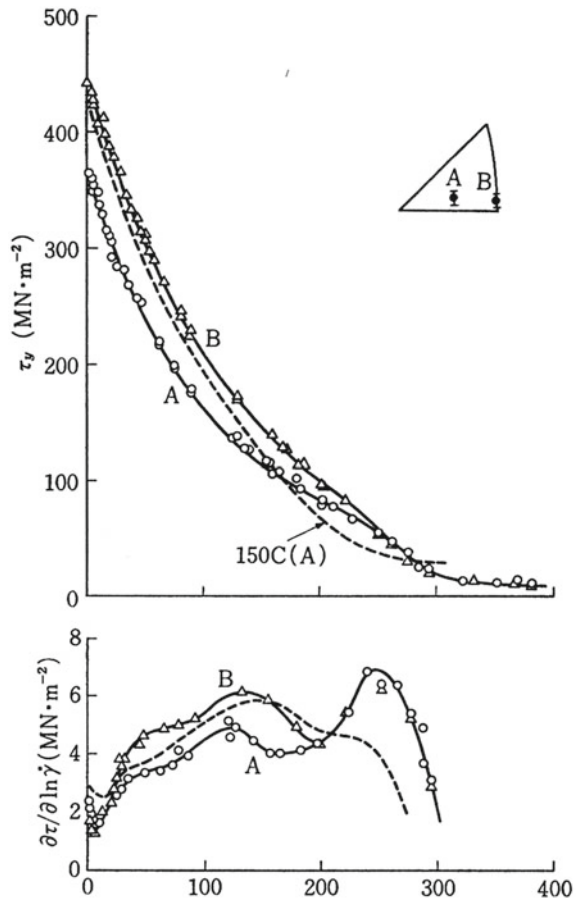
On the other hand, Fig. 8.17 shows the results of the yield stress of pure iron single crystal and its strain rate dependence (Aono et al. 1981). The yield stress at room temperature and its strain rate dependence can be read as 20 and 3 MPa, respectively. Substituting them into Eq. (8.17), the m value is calculated to be approximately 7. Note that this value agrees well with that obtained from the plot shown in Fig. 8.16. These results are the first real-time demonstration of the Johnston–Gilman model, which expresses the relation between dislocation density and flow stress, and it can be said that the elementary process of the relation between dislocation behavior and mechanical response is approached by the new observation and analysis technology.

8.4.3 Plasticity Induced by Phase Transformation

Indentation-induced phase transformation is another important behavior during nanoindentation, as reported for various materials (Ahn et al. 2010; Crone et al. 2007; Frick et al. 2006). Phase transformation is detected by SPM imaging of the sample surface after nanoindentation in most cases, and mechanical behavior analysis for the P–h relation is an important approach for investigating this behavior. As a new analytical approach, a transition in the plastic deformation mechanisms is analyzed from the P/h–h plots (Sekido et al. 2011b). The theoretical load with a conical or pyramidal indenter in an elastoplastic deformation is given by the following equation:

$$P_t = ah^2, \tag{8.18}$$

where a is the material constant that depends on the elastic and the plastic properties of a material. Thus, P/h–h plots should show a constant slope corresponding to a when the deformation mode is kept the same during the deformation. Although the actually measured P_m includes the influences of the tip truncation and stiffness of the load frame, expressed by

$$P_m = ah^2 + a_2 h, \tag{8.19}$$

where $a2$ is the constant that is corresponding to the shape of the indenter tip and the stiffness of the load frame (Ohmura et al. 2002). The coefficient $a2$ turns into the y-intercept by the transformation to the P/h–h plots to separate from the parameter a that corresponds to the intrinsic behavior of materials. However, parameter a changes when different deformation modes operate during a plastic deformation. Then, Eq. (8.18) is expressed in the following two ways:

$$P_t = a_e h_e{}^2 \tag{8.20}$$

and

$$P_t = a_p h_p^2, \tag{8.21}$$

where a_e and a_p are constants for elastic and plastic deformation, and h_e and h_p are the elastic and plastic penetration depths, respectively. a_p is proportional to hardness H given by $H = P/A$, where P is the applied load and A is the projected area of contact, which is proportional to h_p^2. As h can be expressed through a simple summation of h_e and h_p (Oliver and Pharr 1992), the relation among a, a_e, and a_p is given by

$$a^{-1/2} = a_e^{-1/2} + a_p^{-1/2}. \tag{8.22}$$

Assuming that a_e, which is correlated with Young's modulus, is not associated with plastic strain, only a_p is the controlling factor for a in Eq. (8.18). Hence, a slope change on a P/h–h plot corresponding to a in Eq. (8.19) denotes a change in a_p, which is affected by the plastic deformation mode and indicates that a load for the transition of deformation modes can be visualized by the slope change on the P/h–h curve.

Figure 8.18a–c represents the typical P–h curves obtained from the nanoindentation tests under peak loads of 1, 4, and 8 mN. A sudden displacement burst, which is called a pop-in, is observed on the P–h curves, shown as insets in the upper left corner of the figure. The critical load at which the first pop-in occurs is indicated as P_c and the corresponding excursion depth is denoted as Δh. The broken lines in the three figures correspond to the calculated curves from Eq. (8.1), which are obtained by substituting $E^* = 200$ GPa and $R_i = 230$ nm. The experimental data below P_c agree with the calculated curves, suggesting a purely elastic deformation below P_c. Figure 8.18d–f exhibits the P/h–h plots calculated from Fig. 8.18a–c, respectively. The slopes of the P/h–h plots are approximately 0.06 μN/nm^2 at an early stage of plastic deformation, following the first pop-ins that occur below 1 mN, as shown in Fig. 8.18d–f. The slopes of approximately 0.10 μN/nm^2 appear through a further loading of up to 4 and 8 mN, as shown in Fig. 8.18e, f. This slope change on the
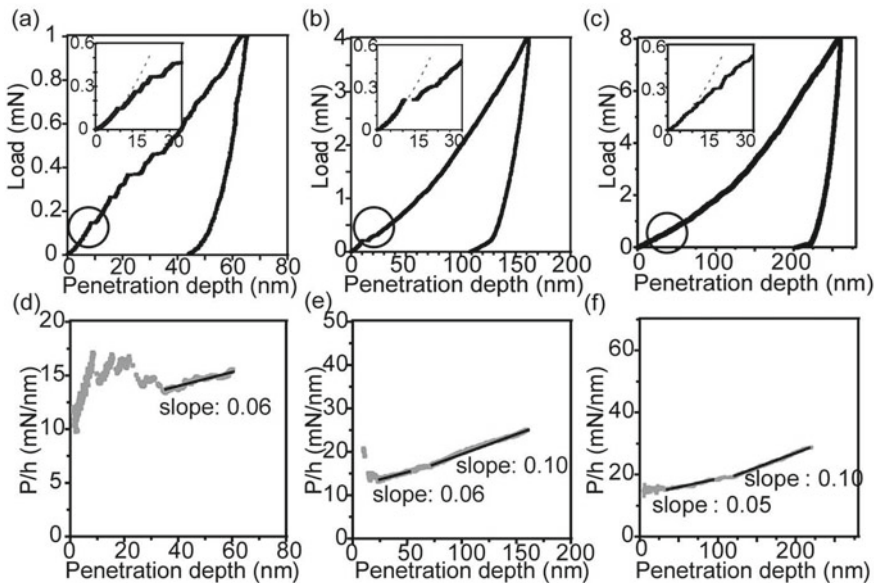
Fig. 8.18 P–h curves obtained by nanoindentation with peak loads of **a** 1 mN, **b** 4 mN, and **c** 8 mN. The P–h curves (**a**), (**b**), and (**c**) after the first pop-ins are converted into P/h versus h curves of **d** 1 mN, **e** 4 mN, and **f** 8 mN, respectively (Sekido et al. 2011b). Reprinted with permission from [K. Sekido, T. Ohmura, T. Sawaguchi, M. Koyama, H.W. Park and K. Tsuzaki: Scripta Mater., 65 (2011), 942–945.] Copyright (2011) by Elsevier
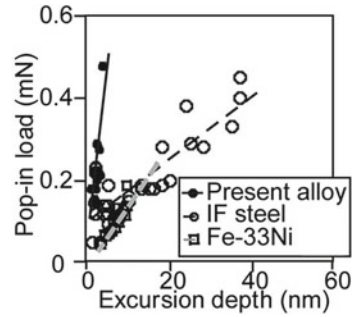
P/h–h curves is speculated to be the consequence of the change in the predominant deformation mode.

The SPM observations indicate that the stress-induced ε-martensitic transformation is the deformation mode that predominantly operates at an early stage of plastic deformation during nanoindentation (Sekido et al. 2011b). Figure 8.19 shows the relation between the critical load P_c and the corresponding excursion depth Δh at the first pop-in. The results for an Fe-33Ni steel (FCC) and a Ti-added IF steel (BCC) are also shown for comparison. The figure shows that based on equivalent P_c values, the values of Δh in the present alloy are significantly smaller than those in the IF and Fe–Ni steels. P_c and Δh have been shown to be closely related to their Young's moduli (Ohmura and Tsuzaki 2007b); however, Young's modulus of the present alloy is comparable to that of the IF and Fe–Ni steels, suggesting that the smaller values of Δh cannot be attributed to the elastic property. Note that the present alloy shows the stress-induced ε-martensitic transformation at a lower load (Otsuka et al. 1990), while the slip deformation has been identified as the predominant deformation mode in IF and Fe–Ni steels, at least on a bulk scale. Therefore, a smaller Δh is derived from the deformation mode operating in the present alloy, i.e., the stress-induced ε-martensitic transformation. Using the geometrically necessary (GN) dislocation loop model proposed by Shibutani et al. (Shibutani et al. 2007), the excursion depth Δh is given as

$$\Delta h = nb, \tag{8.23}$$

where n is the number of GN dislocations. Equation (8.23) shows that a smaller Δh corresponds to fewer dislocations formed during the pop-in event. ε-martensite is known to form by the motion of partial dislocations on alternative {111} planes. As the dislocation multiplication in FCC metals requires the shrinkage of extended dislocations, no dislocation multiplication occurs during the stress-induced ε-martensitic transformation. Thus, the smaller Δh in the present alloy also implies the occurrence of ε-martensitic transformation.

In a practical design of high-performance steel by phase transformation, the transformation-induced plasticity (TRIP) effect is a major factor for maintaining

a good balance between strength and elongation (Cooman 2004; Aydin et al. 2013; Cao et al. 2011; Zaefferer et al. 2004; Jacques 2004; Zackay et al. 1967). The stability of austenite phase is affected by many factors, including chemical composition, grain size, grain geometrical shape, crystallographic orientation, and the phase surrounding the retained austenite, and further understanding of individual factors is required. To address this issue, nanoindentation techniques are applied to investigate the mechanical stability of individual retained austenite grains in TRIP steels, especially for the boundary effect.

Nanoindentation tests are performed for the austenite grains with different size in high-carbon quenched-tempered steel (Man et al. 2019). Figure 8.20 presents the phase maps and SPM images of the three austenite grains, which is highlighted by dashed lines. The corresponding P/h–h plots for the three grains are presented in Fig. 8.21. Interestingly, all P/h–h plots show double stages on the loading curve during the plastic deformation, i.e., slope a with a low value for in stage I turns into a higher value in stage II. In addition, the value of a in stage I is higher for the small grains. Furthermore, the transition load P_t, which is defined as the change in the slope of the P/h–h plot, is found to increase with decreasing the austenite grain size. In fact, the slope a in stage I is lower and the P_t value is relatively clear for a large austenite grain. In contrast, a is larger in stage I, and thus P_t is difficult to determine for a small austenite grain. For getting a reliable conclusion, the nanoindentation tests were repeated for 76 austenite grains with different sizes. Thus, Fig. 8.22a, b shows plots of slope a in stage I and the P_t value, respectively, as a function of austenite grain size D. As indicated, when the austenite grain size increases, both the slope a in stage I and the P_t value decrease. Although the data show some scattering due to the irregular shapes of the austenite grains, it is concluded that larger grain size has lower resistance to plastic deformation. A change in the slope of the P/h–h plot is believed to be the consequence of a change in the deformation mode for the plastic deformation in the retained austenite, which is a transition from the stress/strain-induced martensitic transformation of the metastable retained austenite into the dislocation glide motion in the transformed martensite. It is also found that both the slope a in stage I and the value of P_t increase upon decreasing the austenite grain size. This result suggests that the mechanical stability of the retained austenite increases with decreasing grain size, that is, the resistance against stress-induced martensitic transformation increases in smaller grained austenite. This can be partly attributed to a constraint effect by the surrounding tempered martensite phase. As the tempered martensite phase is harder than the retained austenite phase, the austenite to martensite transformation with volume expansion should be inhibited by the tempered martensite phase. This effect is more significant in a region close to the interface because the volume expression by the γ to α' transformation is subjected to greater compressive stresses and space limitations from the martensite–austenite interface in smaller austenite grains.

The boundary effect on the mechanical stability of metastable austenite (γ) in the Fe–Ni steels is characterized using a combination of nanoindentation and transmission electron microscopy (Man et al. 2020). Figure 8.23a, c shows phase maps drawn after the nanoindentation tests, where red and green indicate γ and α', respectively. Figure 8.23b, d shows the corresponding Image Quality maps. Nanoindentation tests
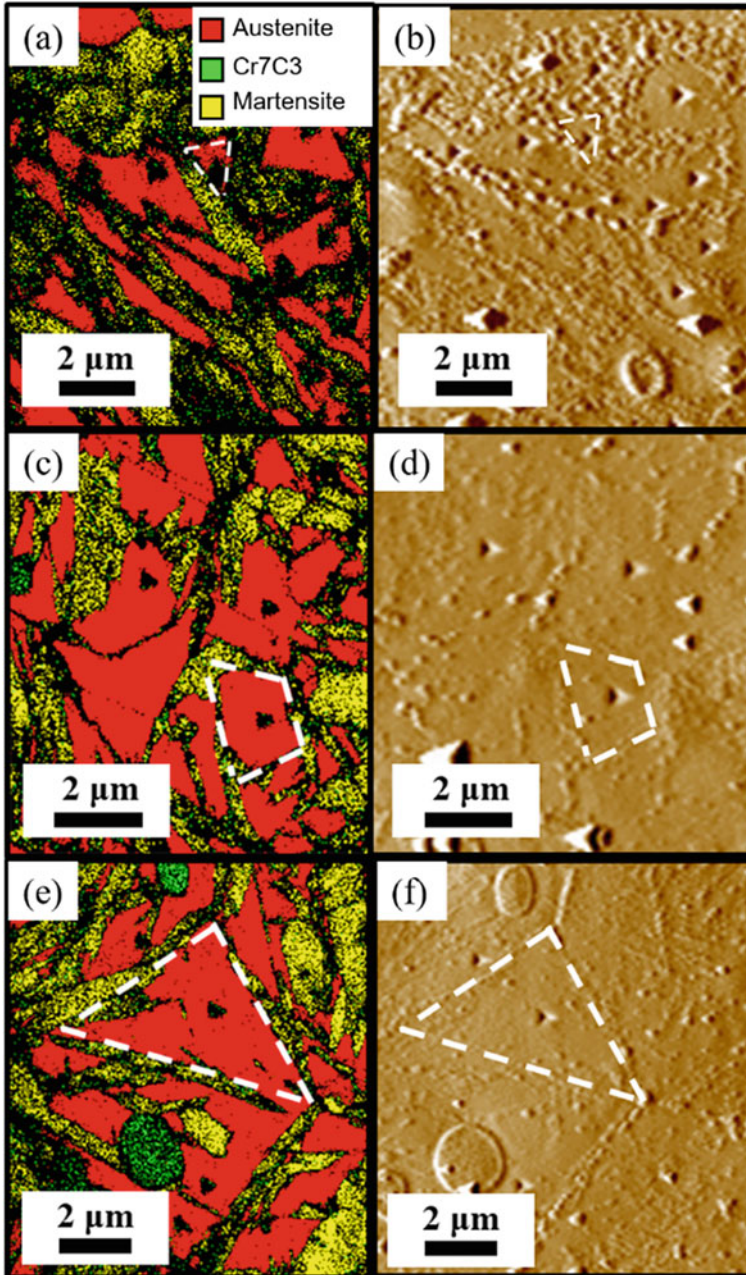
Fig. 8.20 a Phase map and **b** SPM image showing the indentation mark position in the retained austenite grain with a smaller grain size of 1.55 µm indicated by dashed triangle. **c, d** The middle size of 2.76 µm indicated by dashed quadrangle, and **e, f** a larger size of 5.38 µm indicated by dashed triangle (Man et al. 2019). Reprinted with permission from [T. Man, T. Ohmura and Y. Tomota: ISIJ Int., 59 (2019), 559–566.] Copyright (2019) by The Iron and Steel Institute of Japan

Fig. 8.21 *P/h* versus *h* plots corresponding to the three grains with sizes of **a** 1.55 µm, **b** 2.76 µm, **c** 5.38 µm shown in Fig. 8.6. All plots exhibit the two stages of I (blue) and II (green) (Man et al. 2019). Reprinted with permission from [T. Man, T. Ohmura and Y. Tomota: ISIJ Int., 59 (2019), 559–566.] Copyright (2019) by The Iron and Steel Institute of Japan
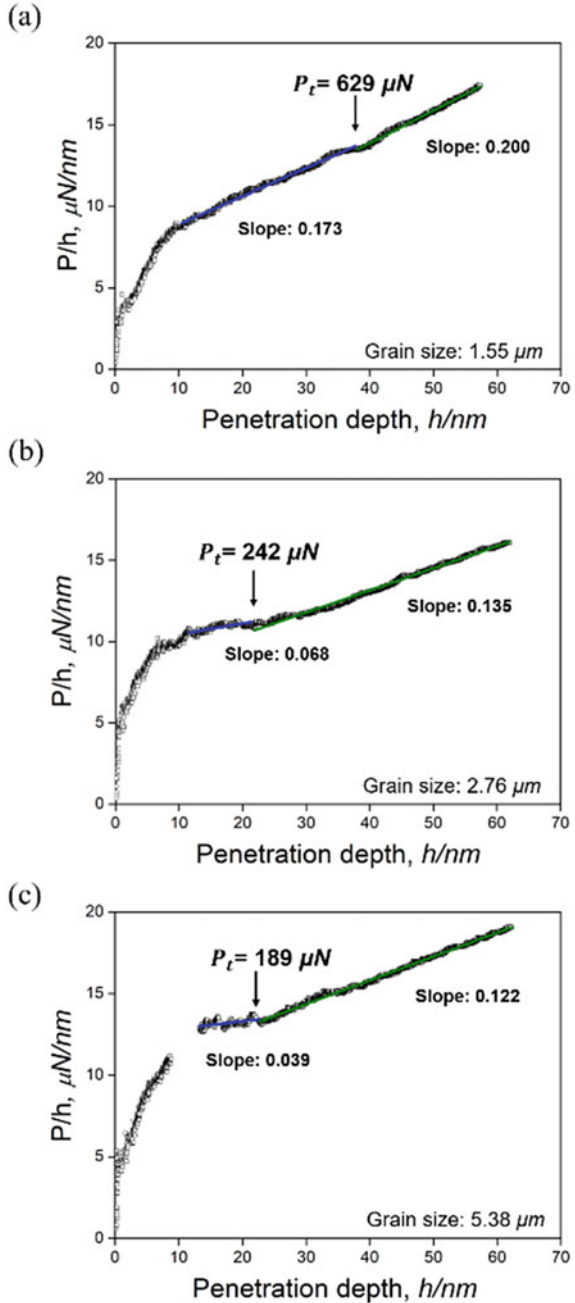
Fig. 8.22 **a** Slope a in stage I and **b** the transition load P_t plotted as a function of the grain size D of retained austenite phase (Man et al. 2019). Reprinted with permission from [T. Man, T. Ohmura and Y. Tomota: ISIJ Int., 59 (2019), 559–566.] Copyright (2019) by The Iron and Steel Institute of Japan
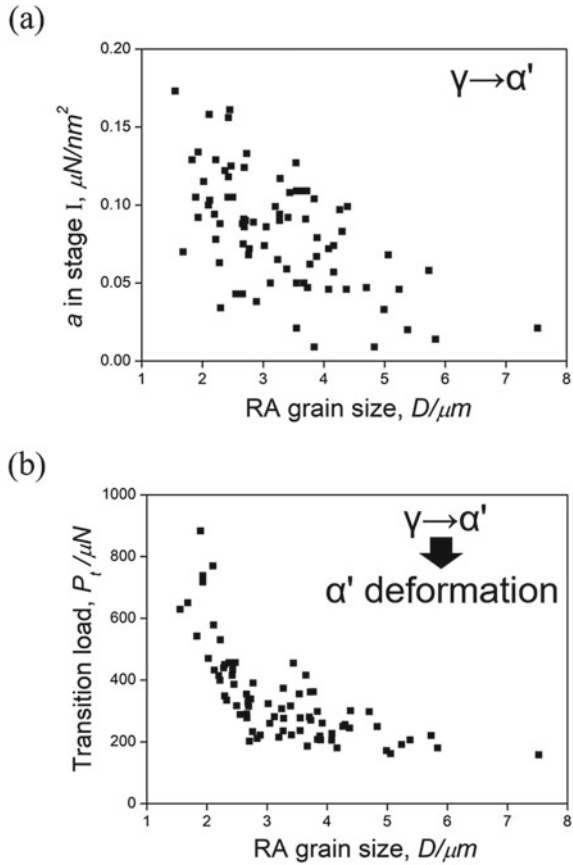
with a peak load of 2000 μN are conducted within the γ grain interior and in the vicinity of the γ/γ grain boundary, as well as the γ/α' interface. The indentation marks at the γ grain interior, in the vicinity of the γ/γ grain boundary, as well as the γ/α' interface, are outlined by pink, orange, and blue circles and arrows, respectively, as shown in Fig. 8.23b, d. Figure 8.24 shows a plot of the average values of slope a on $P/h - h$ plot in stage I and P_t for metastable γ in Fe-27Ni and the stable γ in Fe-30Ni. The plot includes the results for the γ grain interior, γ/γ grain boundary, and γ/α' interface, which are indicated by rectangles, circles, and rhombi, respectively. In each case, the error bars are calculated on the basis of SDs for the total data. The results show a tendency for the average values of slope a in stage I and of P_t for metastable γ to become lower for the γ/α' interface, γ/γ grain boundary, and γ grain interior, in turn. Furthermore, the average slope of the a value for the γ grain interior is lower in stage I of metastable γ in Fe-27Ni (0.013 μN/nm^2) than in the plastic deformation stage of stable γ in Fe-30Ni (0.025 μN/nm^2). In addition, the difference in the average slope values between the γ/γ grain boundary and γ grain interior is higher for metastable γ in Fe-27Ni (0.012 μN/nm^2) than that for stable γ in Fe-30Ni
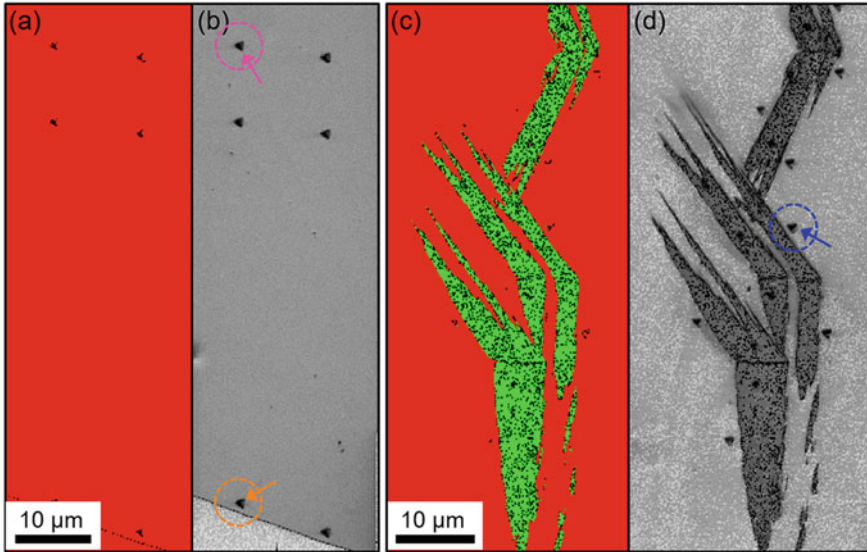
Fig. 8.23 **a**, **c** Phase maps, where red indicates austenite (γ) and green indicates martensite (α'), and **b**, **d** IQ maps taken after nanoindentation tests with a peak load of 2000 μN. The indentation marks at the γ grain interior and in the vicinity of the γ/γ grain boundary in Fe-27Ni-H, and in the vicinity of the γ/α' interface in Fe-27Ni-S, are outlined by the pink, orange, and blue circles and arrows in (**b**) and (**d**), respectively (Man et al. 2020). Reprinted with permission from [T. Man, T. Ohmura and Y. Tomota: Mater. Today Comm., 23 (2020), 100896] Copyright (2020) by Elsevier
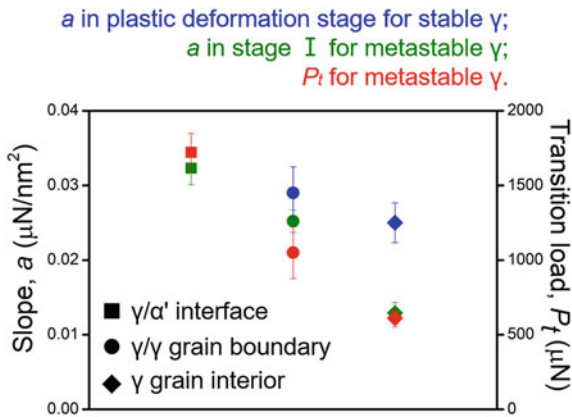
Fig. 8.24 Plot of average values of slope a in stage I and P_t for metastable γ in Fe-27Ni-H and Fe-27Ni-S, and slope a in plastic deformation stage for stable γ in Fe-30Ni, where γ grain interior, γ/γ grain boundary, and γ/α' interface are indicated by rectangles, circles, and rhombi, respectively. Error bars are calculated based on standard deviation for total data in each case (Man et al. 2020). Reprinted with permission from [T. Man, T. Ohmura and Y. Tomota: Mater. Today Comm., 23 (2020), 100896] Copyright (2020) by Elsevier

(0.004 μN/nm^2). The average values of slope a in stage I and P_t for the γ/γ grain boundary and γ/α' interface are higher than those for the γ grain interior, indicating that the resistance of the boundaries to martensitic transformation is higher than that in the γ grain interior. Furthermore, the average values of slope a in stage I and P_t for the γ/α' interface are higher than those for the γ/γ grain boundary, suggesting that the constraint effect of the γ/α' interface is higher than that of the γ/γ grain boundary, as the hardness of α' is higher than that of γ.

8.5 Summary

This chapter introduces nanoindentation and TEM in situ deformation analysis, which are a method for directly analyzing the mechanical behavior on nanoscale and capturing the relation with dislocation motion in real time. The new analysis method enables us to grasp the behavior on the nanoscale in detail, and new knowledge is obtained on the function of grain boundaries as dislocation sources, the deformation behavior related to dislocation motion other than viscous motion, and the relation between the character of dislocation and mechanical response. To clarify the mechanism of plastic phenomena in more detail, it is necessary to reveal the effect of temperature, which is an important external state variable, as well as stress, and it is desired to improve the measuring technique at low temperatures below room temperature, or conversely, at high temperatures. To overcome the 10^6 order gap mentioned in the Introduction, it is necessary to construct a material behavior model based on the new knowledge. This is a barrier that could not be completely overcome even by the conventional dislocation theory, but we would like to continue challenging it further through advanced efforts, such as new experimental analysis methods.

A new concept of "*Plaston*" was proposed for further understanding the mechanical behavior and controlling the performance of structural materials (Tsuji et al. 2020). *Plaston* presumably include a singularity with a stress intensity and an excited state with elastic strain energy leading to a mechanically instability in a local atomistic arrangement. It is expected that the unstable state instantaneously transfers to metastable states in various lattice defects including dislocations, twin defects, cracks, phase boundaries and so on. As the transferred defects subsequently dominate the macroscopic mechanical properties of materials, it is important to control a transition path to choose an appropriate defect structure. That is a novel guide principle to get high-performance materials. The mechanical singularity presumably occurs at local regions such as crack tip, grain boundary, triple junction etc., which can hardly be captured by conventional experimental approach. For the issuers, the nanoindentation has a strong potential by inducing an excited state intentionally at any positions in a material to see how materials behave under the unstable state. In particular, the pop-in event, which is described in this chapter, is an interesting phenomenon under a remarkably high-stress state close to the theoretical strength level. Therefore, nanomechanical characterization has a great potential to reveal an elementally step of various deformation modes and develop the concept of *Plaston*.

References

Ahn TH, Oh CS, Kim DH, Oh KH, Bei H, George EP, Han HN (2010) Scripta Mater 63:540–543

Aono Y, Kuramoto E, Kitajima K (1981) Rep Res Inst Appl Mech Kyu-shu Univ XXIX:127

Aydin H, Essadiqi E, Jung I, Yue S (2013) Mater Sci Eng A 564:501

Bolshakov A, Pharr GM (1998) J Mater Res 13:1049

Brenner SS (1956) J Appl Phys 27:1984

Britton TB, Randman D, Wilkinson AJ (2009) J Mater Res 24:607–615

Cao WQ, Wang C, Shi J, Wang MQ, Hui WJ, Dong H (2011) Mater Sci Eng A 528:6661

Carpeno DF, Ohmura T, Zhang L, Leveneur J, Dickinson M, Seal C, Kennedy J, Hyland M (2015) Mater Sci Eng A639:54–64

Carrington WE, McLean D (1965) Acta Matell 13:493–499

Chung T-F, Yang Y-L, Huang B-M, Shi Z, Lin J, Ohmura T, Yang J-R (2018) Acta Mater 149:377–387

Cottrell AH, Bilby BA (1949) Proc Phys Soc Sect A 62:49–62

Crone WC, Brock H, Creuziger A (2007) Exp Mech 47:133–142

De Cooman BC (2004) Curr Opin Solid State Mater Sci 8:285

Doerner MF, Nix WD (1986) J Mater Res 1:601

Edagawa K, Suzuki T, Takeuchi S (1997) Phy Rev B 55:6180

Frick CP, Lang TW, Spark K, Gall K (2006) Acta Mater 54:2223–2234

Gerberich WW, Nelson JC, Lilleodden ET, Anderson P, Wyrobek JT (1996) Acta Mater 44:3585–3598

Gouldstone A, Koh H-J, Zeng K-Y, Giannakopoulos AE, Suresh S (2000) Acta Mater 48:2277–2295

Hall EO (1951) Proc R Soc B64:747–753

Hauser JJ, Chalmers B (1961) Acta Matell. 9:802–818

Hirsch PB (1968) Suppl Trans JIM 9:XXX

Hsieh Y-C, Zhang L, Chung T-F, Tsai Y-T, Yang J-R, Ohmura T, Suzuki T (2016) Scripta Mater 125:44–48

Itokazu M, Murakami Y (1993) Trans Jpn Soc Mech Eng A 59:560

Jacques PJ (2004) Curr Opin Solid State Mater Sci 8:259

Johnson KL (1985) Contact mechanics. Cambridge University Press, Cambridge, UK, pp 84–106

Johnston WG (1962) J Appl Phys 33:2716

Johnston WG, Gillman JJ (1959) J Appl Phys 30:129

Kim Y-J, Yoo B-G, Choi I-C, Seok M-Y, Kim J-Y, Ohmura T, Jang J-I (2012) Mater Lett 75:107–110

Kurzydlowski KJ, Varin RA, Zielinski W (1984) Acta Metall 32:71–78

Lee TC, Robertson IM, Birnbaum HK (1990) Met Trans 21A:2437–2447

Leipner HS, Lorenz D, Zeckzer A, Lei H, Grau P (2001) Physica B 308–310:446–449

Li JCM (1963) Trans AIME 227:239–247

Lim YY, Chaudhri M (1999) Phil Mag A 79:2979

Lorenz D, Zeckzer A, Hilpert U, Grau P, Johansen H, Leipner HS (2003) Phys Rev B 67:172101

Loubet JL, Georges JM, Marchesini JM, Meille G (1984) J Tribl 106:43

Man T, Ohmura T, Tomota Y (2019) ISIJ Int 59:559–566

Man T, Ohmura T, Tomota Y (2020) Mater Today Comm 23:100896

Masuda H, Morita K, Ohmura T (2020) Acta Mater 184:59–68

McElhaney KW, Vlassak JJ, Nix WD (1998) J Mater Res 13:1300

Minor AM, Asif SAS, Shan Z, Stach EA, Cyrankowski E, Wyrobek TJ, Warren OL (2006) Nat Mater 5:697–702

Nakano K, Ohmura T (2020) J Iron Steel Inst Japan 106:82–91

Newey D, Willkins MA, Pollock HM (1982) J Phys E Sci Instrum 15:119

Nishibori M, Kinoshita K (1978) Thin Solid Films 48:325

Nishibori M, Kinoshita K (1997) Japan. J Appl Phys 11:758

Nix WD, Gao H (1998) J Mech Phys Solids 46:411

Ohmura T, Tsuzaki K (2007a) Materia Japan 46:251

Ohmura T, Tsuzaki K (2007b) J Mater Sci 42:1728–1732

Ohmura T, Tsuzaki K (2008) J Phys D 41:1–6

Ohmura T, Matsuoka S, Tanaka K, Yoshida T (2001) Thin Solid Films 385:198–204

Ohmura T, Tsuzaki K, Matsuoka S (2002) Phil Mag A 82:1903–1910

Ohmura T, Tsuzaki K, Tsuji N, Kamikawa N (2004a) J Mater Res 19:347–350

Ohmura T, Minor A, Stach E, Morris JW Jr (2004b) J Mater Res 19:3626–3632

Ohmura T, Tsuzaki K, Yin F (2005) Mater Trans 46:2026–2029

Ohmura T, Zhang L, Sekido K, Tsuzaki K (2012) J Mater Res 27:1742–1749

Oliver WC, Pharr GM (1992) J Mater Res 7:1564

Onose K, Kuramoto S, Suzuki T, Chang Y-L, Nakagawa E, Ohmura T (2019) J Jpn Inst Light Metals 69:273–280

Otsuka H, Yamada H, Maruyama T, Tanahashi H, Matsuda S, Murakami M (1990) ISIJ Int 30:674

Petch NJ (1953) J Iron Steel Inst 174:25–28

Sato Y, Shinzato S, Ohmura T, Ogata S (2019) Int J Plast (In Press)

Schuh CA, Mason JK, Lund AC (2005) Nat Mater 4:617

Sekido K, Ohmura T, Zhang L, Hara T, Tsuzaki K (2011a) Mater Sci Eng A 530:396–401

Sekido K, Ohmura T, Sawaguchi T, Koyama M, Park HW, Tsuzaki K (2011b) Scripta Mater 65:942–945

Sekido K, Ohmura T, Hara T, Tsuzaki K (2012) Mater Trans 53:907–912

Shen Z, Wagoner RH, Clark WAT (1988) Acta Metall 36:3231–3242

Shibutani Y, Koyama A (2004) J Mater Res 19:183–188

Shibutani Y, Tsuru T, Koyama A (2007) Acta Mater 55:1813

Stein DF, Low JR (1960) J Appl Phys 31:362

Suzuki H (1968) Dislocation dynamics, Rosenfield AR, Hahn GT, Bement AL, Jaffee RI (eds). McGraw Hill, New York:679–700

Suzuki T,. TakeuchiT (1989) Lattice defects in ceramics, Takeuchi S, Suzuki T (eds). Publication office of Japanese journal of applied physics. Tokyo, p 9

Takeuchi S (1981) Intermetallic potentials and crystalline defects, Lee JK (ed). The metallurgical society of AIME, pp 201–221

Takeuchi S, Suzuki T (1989) Strength of metals and alloys, Kettunen PO, Lepisto TK, Lehtonen ME (eds). Pergamon Press, Oxford, p 161

Tsui TY, Oliver WC, Pharr GM (1996) J Mater Res 11:752

Tsuji N, Ogata S, Inui H, Tanaka I, Kishida K, Gao S, Mao W, Bai Y, Zheng R, Du J-P (2020) Scripta Mater 181:35

Uchic MD, Dimiduk DM, Florando JN, Nix WD (2004) Science 305:986

Ushioda K, Takata K, Takahashi J, Kinoshita K, Sawada H (2019) J Jpn Inst Metals 83:353 (in Japanese)

Vitek V (1974) Cryst Lattice Defects 5:1

Zackay VF, Parker ER, Fahr D, Busch R (1967) Trans ASM 60:252

Zaefferer S, Ohlert J, Bleck W (2004) Acta Mater 52:2765

Zbib AA, Bahr DF (2007) Metall. Mater Trans 38A:2249–2255

Zhang L, Ohmura T, Emura S, Sekido N, Yin F, Min X, Tsuzaki K (2009) J Mater Res 24:2917–2923

Zhang L, Ohmura T, Sekido K, Nakajima K, Hara T, Tsuzaki K (2011) Scripta Mater 64:919–922

Zhang L, Ohmura T, Sekido K, Hara T, Nakajima K, Tsuzaki K (2012) Scripta Mater 67:388–391

Zhang L, Ohmura T (2014) Phys Rev Lett 112:145504

Zhang L, Sekido N, Ohmura T (2014) Mater Sci Eng A611:188–193